In This Issue:

Departments

News Briefs and Reports

Conferences/Events

Articles

News Briefs and Reports

Developments

NBS MAKES OPERATIONAL HIGH-TEMPERATURE SUPERCONDUCTING DEVICE

NBS scientists have demonstrated what may be the first superconducting electronic device to operate at 81 kelvins—above the liquid nitrogen temperature of 77 K. The superconducting quantum interference device, or SQUID, is a high-temperature version of the most sensitive existing device for measuring magnetic fields. In the future these high-temperature devices may replace important elements of the common electrocardiograph, and be used for prospecting and in computers.

James E. Zimmerman, a recently retired NBS physicist now working in the Bureau's Boulder laboratories as a guest researcher, designed and constructed the SQUID. Zimmerman is internationally known for his work on superconducting devices and the refrigerators used to cool them.

The yttrium-barium-copper oxide material, which permitted the device to operate up to 81 K, was made at NBS by Ronald Ono and James Beall. Because of the relatively high operating temperature of the SQUID, there was no need to reduce the pressure of the liquid nitrogen, an expensive process sometimes needed to cool the nitrogen below 77 K.

In another development at NBS, John Moreland and Alan Clark observed the ac Josephson effect above 77 K, confirming that electrons in these new materials are paired as they are in conventional superconductors. Devices based on this effect may become future microwave detectors and sources, and voltage standards.

The National Bureau of Standards has conducted research on superconductivity for many decades.

Scientists at NBS have achieved record-setting performance with superconducting electronic devices, applying them in standards and electrical measurements. They also have worked with industry and universities in superconducting device applications in biomagnetism and geophysics, as well as in basic physics.

In addition, Bureau scientists have helped industry to develop superconducting wires and magnets, contributing through standards development and research to understand their operation.

For further information, contact any of the above-named researchers at the National Bureau of Standards, Boulder, CO 80303.

FIRST ENERGY GAP MEASUREMENTS ON SUPERCONDUCTOR MATERIALS

Using a recently developed break junction technique, NBS researchers have made the first electron tunneling measurements of the energy gap in one of the new superconductor materials with relatively high critical temperatures (T_c). The material was lanthanum-strontium-copper oxide, which becomes superconducting at 36 K, and is similar to other materials recently discovered with T_c's as high as 98 K. The energy gap in La-Sr-Cu-O$_4$ was found to be 7.0 ± 0.1 meV. This measurement provided the first glimpse at the microscopic quantum nature of the superconductivity in these new high-T_c materials. Until recently superconductivity was a phenomenon observed only at temperatures below about 20 K, where refrigeration costs are very high. Several materials have now been discovered with T_c's up to five times as high, allowing the substitution of liquid nitrogen (at 77 K) for helium as a refrigerant, lowering costs by a huge factor.

For further information, contact J. M. Moreland or A. F. Clark, National Bureau of Standards, Boulder, CO 80303.

NBS REPORT TO CONGRESS ON U.S. EMBASSY BUILDING IN MOSCOW: STRUCTURAL DEFICIENCIES EXIST BUT CAN BE CORRECTED

The new U. S. Embassy Office Building under construction in Moscow has important structural deficiencies, but the costs to remedy these deficiencies would be modest in comparison to the total construction project. This was the conclusion reached by NBS researchers in a report to Congress.

Last spring, NBS was directed by Congress to assess and report on the current structure and to provide recommendations and cost estimates for correcting structural flaws and defects.

The NBS report to Congress states that remedial measures required to assure the safety of occupants do not involve major reconstruction. It concludes that if similar repairs were done in Washington, DC, the corrective measures could be completed in less than a year and would cost an estimated $1.83 million. Actual costs of the recommended measures would depend greatly upon working conditions in Moscow and the way in which the work was performed, according to the report.

As directed by Congress, NBS investigated only the structural integrity of the building and did not consider security aspects.

NBS concluded that "important deficiencies exist in the structure that must be corrected for adequate safety before the building is occupied."

These deficiencies include joints in reinforced concrete columns and in walls which are not completely filled with the grout and concrete needed to give them full strength. They also include cracking in the roof-top parapet walls. In addition, the NBS research team recommended measures to protect against progressive collapse, which occurs when the failure of a single structural component leads to wider failures within the structure.

NBS assessed the embassy building using criteria consistent with good practice for construction of U.S. office buildings as set out in widely used U.S. voluntary industry standards. In conducting the study, the NBS team reviewed design and construction documents for the site and building, made two visits to Moscow to investigate structural aspects of the building, and conducted tests both at the site and in NBS laboratories in Gaithersburg, MD.

NBS is not a regulatory agency and does not promulgate building standards or codes. The Bureau does develop the tools and technology to test and improve the performance of structures. Results of its research are provided to voluntary standards organizations, state and local governments, and other federal agencies.

NBS has a long history of investigating structures and has studied several well-publicized building failures. Investigations focus on the technical causes of a structural failure or on potential problems which could lead to failure.

For further information on the Moscow report, write Samuel Kramer, National Bureau of Standards, Gaithersburg, MD 20899, or call 301/975-2302.

DIESEL ENGINE IMPROVEMENTS ARE AIM OF NEW THERMOCOUPLES

More efficient and longer-lasting diesel engines may result from the application of a new type of thermocouple device developed at NBS that monitors critical internal temperatures of these engines. Bureau researchers are experimenting with "thin films" of noble, chemically inactive metals such as platinum and gold. Unlike traditional wire thermocouples, these films are deposited directly onto engine parts and act as sensors to indicate temperature at those points. By having accurate temperature measurements during operation of such diesel engine components as valves, cylinder heads, and piston crowns, it is possible to monitor wear and tear of engine hardware, as well as to provide input for controlling automatic engine functions such as fuel-air mix and timing.

Temperature data also are important in the design phase of modern ceramic-coated diesel engines for decisions such as how thick the engine's insulting ceramic coating should be or what porosity the coating should have. NBS is working with researchers from Purdue University, the Department of Energy, and the National Aeronautics and Space Administration to test the thin-film technology in a ceramic diesel research engine.

For further information, contact Kenneth Kreider, National Bureau of Standards, Gaithersburg, MD 20899.

NDE TECHNIQUE FOR EARLY DETECTION OF PAINTING FLAWS

NBS researchers have developed a sensitive technique to detect and quantify defects in paint on wood or metal surfaces. The technique uses computer image processing in conjunction with either a video or infrared thermography camera. It can be used not only to determine the number, size, and location of defects within a certain area, but also to estimate the total area covered by defects.

Since the information can be stored, a degradation history can be developed which should help in scheduling maintenance and evaluating the performance of the coating system. Concerns which need

to be addressed include how much of a structure should be sampled to accurately estimate its degradation. Another concern is finding the best photographic procedures to detect defects while avoiding shadows and nonuniform lighting which may hide them.

For further information, contact Mary McKnight, National Bureau of Standards, Gaithersburg, MD 20899.

JOINT AGREEMENT WILL EXAMINE IMPROVED CHEMICAL ANALYSES

Dionex Corporation, a major producer of ion chromatographic equipment, has signed a cooperative agreement with NBS that aims to improve methods of separating "transition" elements—metals such as nickel and copper—from chemical samples. These separations are important preludes to chemical tests by traditional analytical methods such as thin film X-ray fluorescence, isotope dilution mass spectrometry, and electrochemistry. A significant benefit of improving ion chromatographic separation techniques is that better quantitation will likely result from follow-up analytical instruments.

Ion chromatography has many applications. Though these include the analysis of botanical and environmental samples, the NBS Dionex research will concentrate on improving tests of biological and biomedical samples—for example, determining reliably if toxic levels of nickel or vanadium are contained in biological tissues exposed to fossil fuel emissions. Dr. Archava Siriraks, a Dionex chemist, will work on the project with Bureau scientists for an anticipated 3 years.

NBS, MARTIN MARIETTA STUDY COMPUTER VISION SYSTEMS

NBS and Martin Marietta Baltimore Aerospace have begun a joint research program to develop a series of advanced computer-vision algorithms using the Parallel Image Processing Engine (PIPE), a specialized image-processing computer invented at NBS. William Hoff of Martin Marietta will work as a Research Associate with NBS on algorithms for stereo analysis, sparse depth maps, 2-D feature extraction—including color and texture as well as geometric features, image flow, and 3-D range information. The algorithms will be applicable to a wide variety of computer vision problems.

NBS-DESIGNED PRECISION VOLTAGE STEP GENERATOR DESCRIBED

A voltage step generator developed at NBS and designed to calibrate transient waveform records and other test instruments is described in a report [1] now available.

Transient waveform recorders measure rapid voltage pulses. They are used for a wide variety of applications including research into the generation of electrical power by particle-beam fusion reactions or simpler operations such as checking automobile engine performance. The NBS step generator will ensure the reliable operation of these instruments.

The 104-page report devotes sections to the step generator's theory of operation, a description of the instrument system, the device's software, operating instructions, and testing.

Reference
[1] NBS TN 1230, A Precision Programmable Step Generator for Use in Automated Test Systems, available from the Superintendent of Documents, U.S. Government Printing Office, Washington, DC 20402 ($5.50 prepaid, order by stock no. 003-003-02786-3).

HISTORY OF NBS RADIO RESEARCH PUBLISHED

A project to compile the definitive history of radio research at NBS has culminated in the publication of the 842-page, hardbound volume [1].

Achievement in Radio is a comprehensive, exhaustive treatment of the accomplishments and people of the Bureau, always set in the context of external events and developments. NBS was only 10 years old, and practical radio only about 25, when NBS made its first official radio measurement in 1911, a calibration of a wavemeter. Achievement in Radio tells the story of NBS's involvement in radio science, from its spark-and-crystal origins to today's integrated circuits, masers, and satellites. The authors write from firsthand knowledge of most of the period covered.

Reference
[1] Achievement in Radio: Seventy Years of Radio Science, Technology, Standards, and Measurement at the National Bureau of Standards, by Wilbert F. Snyder and Charles L. Bragaw, available from the Superintendent of Documents, U.S. Government Printing Office, Washington, DC 20402 ($55 prepaid, order by stock no. 003-003-02762-6).

OMNITAB 80: STATISTICAL ANALYSIS FOR SCIENTISTS

NBS has published a revised user's manual to OMNITAB, the Bureau's statistical software package [1]. OMNITAB 80 was designed for "scientists who are not programmers." It provides a complete, highly integrated programming system that uses a simple, high-level language to perform both simple and complex statistical and numerical analyses—including matrix analyses—of experimental data. OMNITAB 80 includes a large library of tested, reliable routines with extensive capabilities for plotting the results. It was written to be largely

machine independent and can be run in either batch or interactive modes.

Reference

[1] NBS SP 701, OMNITAB 80: An Interpretive System for Statistical and Numerical Data Analysis, available from the Superintendent of Documents, U.S. Government Printing Office, Washington, DC 20402 ($17 prepaid, order by stock no. 003-003-02775-8). Copies of the program OMNITAB 80, furnished on customized magnetic tape, are available for $1,500 through the NBS Office of Standard Reference Data. For further information, contact Shirley Bremer, A337 Administration Building, National Bureau of Standards, Gaithersburg, MD 20899, or telephone 301/975-2845.

GUIDE AVAILABLE FOR MAKING ECONOMIC ENERGY DECISIONS

More than a decade after the first shock from escalating energy prices, many buildings continue to be designed and constructed with little consideration for energy conservation. The resulting cost to building owners and the nation is enormous.

A new guide by NBS researchers will help builders and building designers, owners, and operators find a balance between energy consumption and energy conservation which will result in more cost-effective building [1]. The publication guides the decision maker to ask the right economic questions. It also shows how to structure problems for solution, how to estimate future cash flows, and how to interpret various measures of economic performance. Worksheets, a computer program, and data tables to assist with evaluations are provided in the publication.

Reference

[1] NBS SP 709, Comprehensive Guide for Least-Cost Energy Decisions, available from the Superintendent of Documents, U.S. Government Printing Office, Washington, DC 20402 ($11 prepaid, order by stock no. 003-003 02790-1). In addition, a computer program diskette is available from several vendors for under $20 and will shortly be available from the National Technical Information Service. Diskette ordering information is in the publication.

SEISMIC DESIGN GUIDELINES ISSUED

NBS, as secretariat of the Interagency Committee on Seismic Safety in Construction, has issued guidelines for federal agencies to use in designing and constructing buildings to resist earthquake damage [1]. The report was prepared as part of the National Earthquake Hazards Reduction Program. The guidelines are based on existing voluntary standards, model building codes, and federal regulations. In particular, the technical content is similar to the seismic design requirements of the 1985 Uniform Building Code published by the International Conference of Building Officials. The report includes information on site planning, structural design criteria, structural analysis procedures, and design details as well as design and construction standards for structural materials including steel, concrete, and wood. In addition, it includes nonstructural design requirements, such as protecting against secondary hazards and information on quality control and inspection.

Reference

[1] NBSIR 87-3524, Seismic Design Guidelines for Federal Buildings, available from the National Technical Information Service, Springfield, VA 22161 ($18.95 prepaid, order by PB# 87-161204/AS).

NBS ISSUES REVISED KWIC INDEX OF ENGINEERING STANDARDS

NBS has updated its Key-Word-In-Context (KWIC) Index of U.S. Voluntary Engineering Standards for use by manufacturers, exporters, importers, and others concerned with standards developed by U.S. trade associations and technical and professional societies.

The KWIC index contains more than 28,000 titles of standards developed by approximately 400 U.S. standards organizations. First published in 1971, the revised microfiche index provides the title, date, source, and number of the standard for each entry. Each standard can be found under all significant key words in the title. The date of publication or last revision, the standard number, and an acronym designating the standards-issuing organization appear as a part of each entry.

For information in the KWIC index, contact the National Center for Standards and Certification Information, A629 Administration Building, National Bureau of Standards, Gaithersburg, MD 20899, telephone: 301/975-4040. Microfiche copies of the KWIC index are available for $18 prepaid from the National Technical Information Service, Springfield, VA 22161. Order by PB# 87-133377.

Standard Reference Materials

SECOND COMMERCIAL SPACE-MADE PRODUCT IS NEW MEASUREMENT TOOL FOR CHEMISTS

The second commercial space-made product, Standard Reference Material 1961, 30-Micrometer Polystyrene Spheres, is a new small-particle measurement standard developed for industry by NBS. The reference material is an important quality-control tool for chemists using powders for the manufacture of pharmaceuticals, chemicals, industrial compounds, and other products that require particle sizing near 30 micrometers.

The new SRM is the fourth small-particle material in a series of primary measurement standards NBS is developing in cooperation with ASTM. The Bureau plans to certify other small-particle standards up to 100 micrometers.

SRM 1961 is a 5-milliliter vial with approximately 1 million of the 30-micrometer spheres suspended in water. Like the first commercial space-made product offered by NBS in 1985—SRM 1960, 10-Micrometer Polystyrene Spheres-the new SRM also was made in space by the National Aeronautics and Space Administration (NASA) because a low-gravity environment produces a product that is more uniform in size and shape than earth-bound processes for polystyrene materials of this size.

NASA completed the manufacture of the particles for the new SRM aboard the Space Shuttle Challenger during the STS-11 mission in February 1984 with the same Monodisperse Latex Reactor (MLR) experiment that produced SRM 1960. The MLR experiments use a chemical process developed for NASA by Lehigh University.

The principal investigator for the chemical process was John W. Vanderhoff of Lehigh University's Polymer Emulsion Institutes along with coinvestigators Mohamed S. El-Aasser and Fortunato J. Micale of Lehigh, and Dale M. Kornfeld of the NASA Marshall Space Flight Center.

The 30-micrometer measurement standard was certified by NBS physicists Arie W. Hartman and Theodore T. Doiron, using optical measurement techniques to obtain the average particle diameter. Their certified value was confirmed by Gary G. Hembree using an electron microscope to scan individual particles. Russell C. Obbink, ASTM Research Associate at NBS, coordinated industry participation through the ASTM Coordinating Committee for SRMs for Particle Metrology.

The other small-particle reference standards, available from NBS in 5-milliliter vials, are earth-made spheres measuring 0.3 and 1 micrometers. The 10-micrometer space-made material also is available on a microscope slide (SRM 1965) as an education tool for students and as a standard to calibrate microscopes.

SRM 1961 is available as a 5-milliliter vial with approximately 1 million of the 30-micrometer spheres suspended in water, at a cost of $608.

NEW TEMPERATURE FIXED-POINT SRM: INDIUM

NBS has issued a new Standard Reference Material for temperature based on the freezing/melting point of pure indium. SRM 1971: Indium Freezing-Point Standard supplies a fixed point for temperature calibrations at 156.635 ± 0.002 degrees Celsius on the IPTS-68. The indium point lies near the center of a gap between two other temperature reference points, the freezing points of gallium (30 °C) and tin (232 °C), and so provides an important new point for precision thermometry and temperature control.

SRM 1971 consists of a sealed polytetrafluoroethylene cell containing 100 grams of 99.9999 percent pure indium. The cell has a re-entrant well for temperature measurement. The cost is $655.

IMPROVING CHOLESTEROL, DRUG TESTS IS AIM OF NEW PROGRAM

A "reference laboratory" program, which initially aims to improve clinical measurements of blood serum cholesterol levels and drugs of abuse in urine, has been established by NBS and the 10,450-member College of American Pathologists (CAP).

Both organizations have observed wide variances in clinical test results from laboratories around the country and have worked together for nearly a decade to help improve these often critical measurements. To date, the cooperative research has been devoted to perfecting "definitive" analytical techniques for measuring important blood serum components such as cholesterol, glucose, and uric acid.

The new program expands the joint agreement and places special emphasis on developing affordable reference samples that laboratories can buy and use to check or improve their measurement reliability. The first of these is a kit of freeze-dried human blood serum samples certified for three cholesterol levels. These samples, expected to be available by mid-summer, can be reconstituted as liquids and run through the same tests as patient samples to check equipment operation and methods. NBS and CAP scientists also plan to develop reference samples that would check the accuracy of urinalysis for cocaine abuse.

For further information, contact Harry Hertz, National Bureau of Standards, Gaithersburg, MD 20899.

NBS, VLSI STANDARDS BEGIN JOINT PROGRAM ON LINEWIDTH

NBS and VLSI Standards, Inc. of Mountain View, CA, have begun a joint research program aimed at developing the next generation of linewidth standards for the semiconductor fabrication industry.

Linewidths are an important feature dimension on integrated circuits (ICs). They can be as small as 1 micrometer or below. Proper process control requires the fabricator to be able to measure linewidths accurately, but the problem is compli-

cated because the dimensions of these features are approaching the wavelength of the light used to measure them under a microscope. Determining *exactly* where the edges of the lines are is particularly difficult.

The best current linewidth standards—sold as NBS Standard Reference Materials—are for lines on the photomasks used to make ICs, and depend on light transmitted through the transparent photomask. Equivalent standards are needed for opaque materials such as the silicon IC wafers themselves.

VLSI Standards will develop prototype "artifacts" for NBS consisting of silicon wafers with precisely etched silicon "lines" in relief using a technique to make the walls of the lines as vertical as possible. These artifacts will be used by NBS to correlate physical measurements with optical theory, leading to well-understood techniques for making precise feature measurements on opaque wafers. The samples will also be used in studies to develop similar techniques for scanning electron microscopy.

For further information, contact Robert Larrabee, National Bureau of Standards, Gaithersburg, MD 20899.

tions in the uncertainties for its calibration services for ac/dc thermal voltage and current converters. The highest-accuracy measurements of ac voltage and current are made by reference to well-known dc quantities through thermal converters. Accurate comparisons require calibrating the thermal converter for the difference in response between a dc source and an ac source of equal RMS voltage and current. NBS has lowered the uncertainties in its thermal converter calibration service across most of the audible and higher frequency ranges up to one megahertz, and most of the voltage and current ranges by as much as 50 percent in some cases.

ac/dc thermal converters are the ultimate reference for almost all ac measurements made in the aerospace, defense, and electronics industries, and the market for test equipment making ac current or voltage measurements—over $3 billion in this country last year—is intensely competitive. The improved measurement service should be an important aid to U.S. companies seeking foreign markets.

For further information, write Joseph Kinard, National Bureau of Standards, Gaithersburg, MD 20899, or call 301/975-4250.

NBS Services

SPECIAL TEST SERVICE FOR HELIUM PERMEATION LEAKS

NBS has begun, on a trial basis, a Special Test service for helium permeation leaks. This service offers measurement of leak rates from 10^{-8} to 10^{-11} moles/second (2×10^{-4} to 2×10^{-7} atm cc/s @ 0 °C), and determines the temperature dependence of the leak standard over the range 0 to 50 °C. (The temperature dependence of leak standards is an important—and often unrecognized-factor in their accuracy.)

Initial costs of the service will be assessed on a case-by-case basis, depending on the time involved, and should range from approximately $2000 to $4000. NBS plans to extend the range of the service and offer calibrations for gases other than helium in the future.

Interested parties should write Charles Ehrlich, A55 Metrology Building, National Bureau of Standards, Gaithersburg, MD 20899, or call 301/975-4834.

NBS UPGRADES ac/dc DIFFERENCE CALIBRATIONS

As a result of continuing research and improved instrumentation, NBS has announced major reduc-

MEASUREMENT ASSURANCE FOR THE NUCLEAR POWER INDUSTRY

NBS and the Atomic Industrial Forum (AIF) have begun a new Measurement Assurance Program to aid nuclear power facilities in making accurate measurements of radioactivity. The program, conducted by AIF with assistance from NBS, concentrates on operational and environmental radioactivity measurements (not personnel dosimetry), and includes the distribution of blind standard samples for measurement by participants, analysis of the data from the blind tests, calibration services, technical consulting, and direct traceability to NBS standards.

Utilities representing approximately 40 operating power stations and four commercial laboratories which provide radioactivity standards and calibration services for the nuclear industry already participate in the program. The cost of participating in the program is approximately $10,000 for the first year.

For further information or to enroll in the program, call David Harward, Atomic Industrial Forum, 301/654-9260. For technical details about the program, call Daniel Golas, an AIF research associate at NBS, 301/975-5540.

Sinusoidal Response of dc SQUIDs For rf Power Measurements

Robert L. Peterson

National Bureau of Standards
Boulder, CO 80303

Current, power, and attenuation measurements with rf SQUIDs are based on the fact that the voltage from the microwave readout circuit can be made a nearly sinusoidal function of the magnetic flux threading the SQUID. We point out here that an asymmetric dc SQUID with sufficiently low inductance can achieve a very sinusoidal output voltage with good modulation depth. The spectral purity of the sinusoid can be substantially better than that obtained with rf SQUID systems. The purity improves with increasing asymmetry of the junction critical currents, and decreasing values of the LI_c product, where L is the SQUID inductance and I_c is the smaller of the critical currents. Results of several calculations are presented. Substantial improvement in SQUID methods of rf current, power, or attenuation measurement may thus be possible with use of such dc SQUIDs.

Key words: attenuation; rf-measurements; SQUID; superconductivity.

Introduction

In the early 1970s, Kamper et al. [1–5][1] recognized that superconducting quantum interference devices (SQUIDs), with their periodic response to magnetic flux Φ, had the potential for being used in a completely new kind of current, power, or attenuation measurement. In the systems developed, the rf impedance of a single-junction SQUID (rf SQUID) was measured. The impedance variations were reflected into a resonant circuit and measured as variations in phase or amplitude of the output rf voltage. If the voltage response is purely sinusoidal in flux with period equal to the flux quantum $\Phi_0 = h/2e$,

About the Author: Robert L. Peterson serves with the Electromagnetic Technology Division in the Center for Electronics and Electrical Engineering, NBS.

[1] Numbers in brackets indicate literature references.

$$V = V_0 \cos (2\pi\Phi/\Phi_0), \qquad (1)$$

the time-averaged voltage response to a sinusoidally varying flux of amplitude Φ_m takes the form

$$\bar{V} = V_0 J_0 (2\pi\Phi_m/\Phi_0). \qquad (2)$$

Equation (1) is achieved approximately with use of an overdamped SQUID and a broadband microwave readout circuit [4]. By determining the zeroes of the response experimentally as the flux amplitude is varied, and equating them to the zeroes of the Bessel function J_0, one can determine Φ_m or its equivalent in terms of current.

The periodic response to an impressed flux is, however, not ideally sinusoidal, and this necessitates an elaborate series of corrective procedures [2–7]. The purpose of this note is to point out that a dc SQUID (a superconducting loop containing

two Josephson junctions—see fig. 1) with asymmetric critical currents and sufficiently small inductance and capacitance can have a considerably purer sinusoidal voltage output with adequate modulation. Thus one of the major sources of difficulty in realizing a Josephson junction device for rf measurements can potentially be removed. Although the SQUID inductance is small, the current in the input coil necessary to couple flux into the SQUID can be kept at a reasonable level. The noise in such SQUIDs is also expected to be small.

The *threshold* characteristic (i.e., maximum zero-voltage current *vs.* flux) of a symmetric dc SQUID is not at all sinusoidal. Figure 2 shows an example for a 4-pH SQUID with equal critical currents of 55 μA. It has long been known, however, that the *voltage* developed across a symmetric SQUID has a sinusoidal appearance when the bias current is sufficiently greater than the maximum critical current of the device. This is observed experimentally and from calculations (see, e.g., [8] and references therein).

That an *asymmetric* dc SQUID can exhibit a sinusoidal threshold characteristic has been noted earlier by us [9] as well as by Fulton et al. [10]. No specific application was seen at the time. Intuition suggests, however, that this sinusoidal character should be reflected in the voltage developed across the SQUID, and calculations bear this out, as we shall presently show.

The equations describing the threshold behavior of a dc SQUID are [9]

$$\cos \phi_2 = -\cos \phi_1 / (\alpha + \beta \cos \phi_1), \qquad (3)$$

$$I_m = I_{01} \sin \phi_1 + I_{02} \sin \phi_2, \qquad (4)$$

$$2\pi\Phi/\Phi_0 = \phi_2 - \phi_1 + \beta_2 \sin \phi_2 - \beta_1 \sin \phi_1, \qquad (5)$$

where ϕ_1 and ϕ_2 are the quantum mechanical phase differences across the two Josephson junctions, I_{01} and I_{02} are the respective critical currents, $\alpha = I_{02}/I_{01}$, $\beta_i = 2\pi L_i I_{0i}/\Phi_0$, $\beta = 2\pi L I_{02}/\Phi_0$, $L = L_1 + L_2$, and L_1 and L_2 are the lumped inductances for the two segments of the SQUID. See figure 1. Equation (3) shows that there may not be a real solution for ϕ_2 if the denominator on the right is less than unity. In fact if α and β are each much less than unity, ϕ_2 has
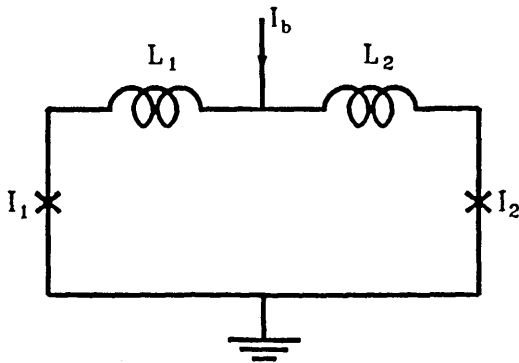
Figure 1—Diagram of a dc SQUID with bias current. The inductances and junctions on the two sides may be different. The crosses represent the junctions, including resistance and capacitance.
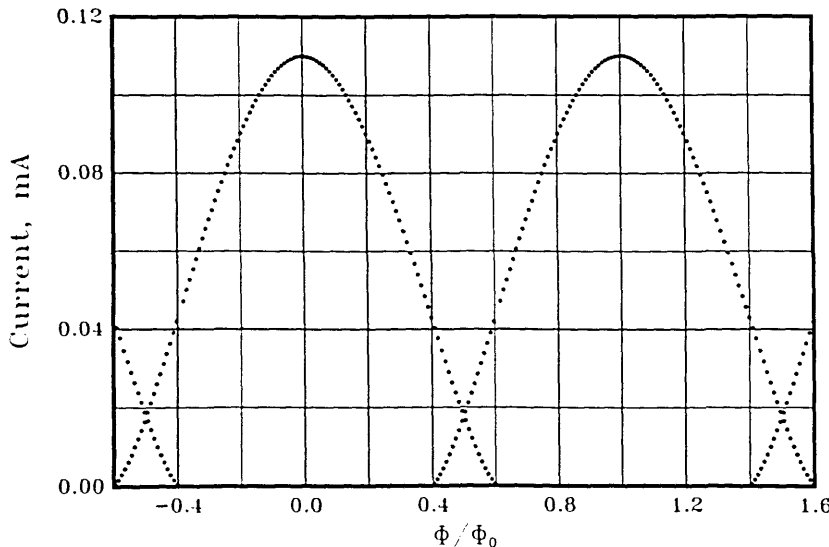
Figure 2—The positive half of the threshold characteristic of a symmetric dc SQUID having $L_1 = L_2 = 2.0$ pH and $I_{01} = I_{02} = 55$ μA.

a solution only for ϕ_1 very close to $(2n+1)\pi/2$ where n is any integer or zero. Choosing $\phi_1 \approx \pi/2$ and noting that the requirements of $\alpha \ll 1$ and $\beta \ll 1$ requires $\beta_2 \ll 1$ (although β_1 may still be of the order of unity), we find from eqs (4) and (5) that

$$I_m \approx I_{01} + I_{02} \sin (2\pi\Phi/\Phi_0 - \beta_2 \sin \phi_2 + \pi/2 + \beta_1)$$

$$\approx I_{01} + I_{02} \cos (2\pi\Phi/\Phi_0 + \beta_1). \qquad (6)$$

This establishes the approximate sinusoidal behavior of the threshold characteristic of a sufficiently asymmetric dc SQUID with low inductance.

In figure 3 we show the computed threshold behavior of an asymmetric dc SQUID, having equal inductances $L_1 = L_2 = 2.0$ pH, and unequal critical currents $I_{01} = 100$ μA, $I_{02} = 10$ μA. We also plot the perfect sinusoid of eq (6) for comparison. Calculations show that the spectral purity of the threshold characteristic can be improved by making the inductances asymmetric as well. This remarkable purity of the threshold characteristic is carried over into the voltage across the SQUID.

The dynamic equations describing a dc SQUID are

$$L_1 C_1 \frac{d^2\phi_1}{dt^2} - L_2 C_2 \frac{d^2\phi_2}{dt^2} + \frac{L_1}{R_1} \frac{d\phi_1}{dt} - \frac{L_2}{R_2} \frac{d\phi_2}{dt}$$

$$+ \phi_1 - \phi_2 + \beta_1 \sin \phi_1 - \beta_2 \sin \phi_2 + 2\pi \frac{\Phi}{\Phi_0} = 0, \qquad (7)$$

$$C_1 \frac{d^2\phi_1}{dt^2} + C_2 \frac{d^2\phi_2}{dt^2} + \frac{1}{R_1} \frac{d\phi_1}{dt} + \frac{1}{R_2} \frac{d\phi_2}{dt}$$

$$+ \frac{\beta_1}{L_1} \sin \phi_1 + \frac{\beta_2}{L_2} \sin \phi_2 = 2\pi \frac{I_b}{\Phi_0}. \qquad (8)$$

Here the C's are the junction capacitances and the R's are resistances shunting the junctions. I_b is the bias current injected as shown in figure 1. To calculate the voltage across the SQUID, we solve eqs (7) and (8) with a fourth-order Runge-Kutta technique. We then time-average over typically 10 cycles to obtain the voltages shown in the figures. The precision of our calculations is estimated as a few parts in 10^5.

In figure 4 we show the calculated time-averaged voltage across the symmetric SQUID of figure 2 for a bias current of 200 μA, about twice the maximum critical current. A sinusoid is also shown for visual comparison. Shunt resistances of 1 Ω and junction capacitances of 0.66 pF are used for the two equal junctions. The junction capacitances are calculated by assuming a current density of 1000 A/cm^2, together with a specific capacitance of 12 μF/cm^2, characteristic of Nb. The voltage modulation at the bias current used is about 11 μV relative to an average voltage of about 90 μV, or about 12 percent modulation.

Figure 5 shows the frequency spectra in decibels for this case as well as for an asymmetric case. The dc component is suppressed. The spectra are obtained by calculating 32 voltage points in one period of the flux, then using a 32-point Fast Fourier Transform (FFT). Unity on the horizontal axis represents the fundamental period Φ_0. The imprecision in the voltage calculations is amplified somewhat in passing through the FFT. Thus, points below
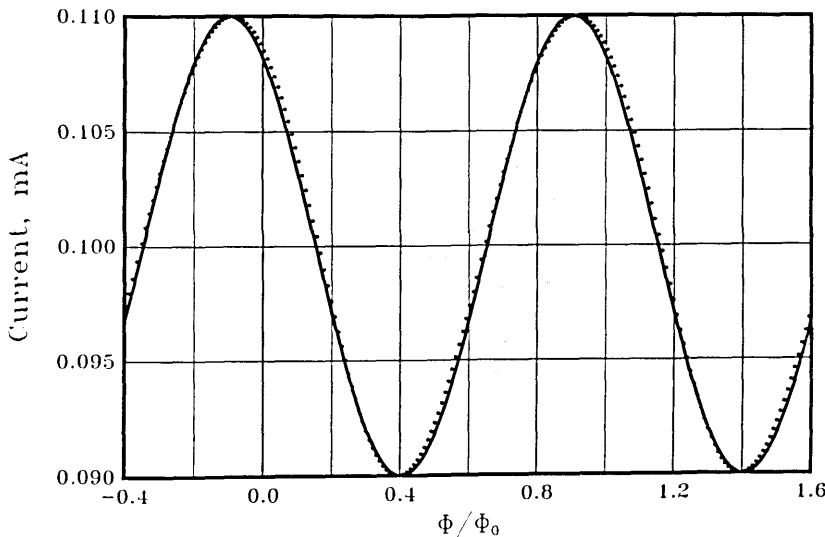
Figure 3—The positive portion of the threshold characteristic of an asymmetric dc SQUID with $L_1 = L_2 = 2.0$ pH, $I_{01} = 100$ μA, $I_{02} = 10$ μA. The solid line is the sinusoid of eq (6) with $\beta_1 = 0.61$.
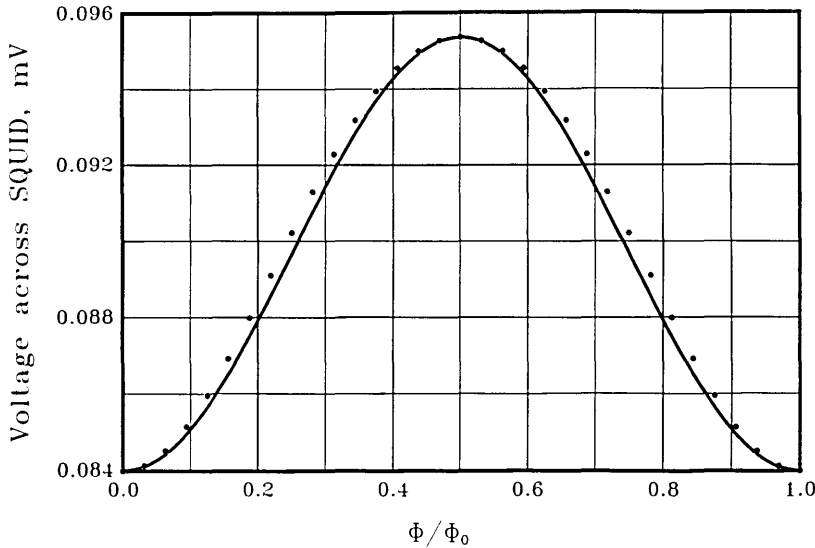
Figure 4—The time-averaged voltage across the symmetric SQUID of figure 2 with a current bias of 200 μA (dots). Shunt resistances of 1 Ω and junction capacitances of 0.66 pF are used. The solid line is a sinusoid for visual comparison.
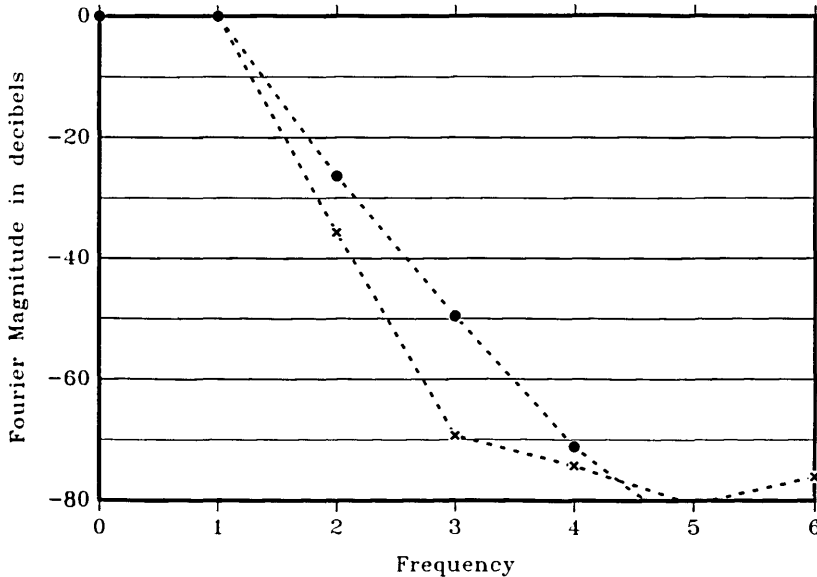
Figure 5—Frequency spectra, in decibels, of the time-averaged voltage across two dc SQUIDs. The solid circles represent the symmetric SQUID of figures 2 and 4. The crosses represent the asymmetric SQUID of figures 3 and 6. The two SQUIDs have the same total inductance and critical current. Levels below about –70 dB are significantly affected by computational noise (see text).

about -70 dB in figure 5 are significantly affected by computational noise.

The solid circles in figure 5 show the spectrum of the symmetric SQUID of figure 4. The spectral purity of the voltage of this SQUID is better than that reported for an rf SQUID [4]. The second harmonic is about 26 dB below (5 percent of) the fundamental, and the third harmonic is 50 dB down (0.3 percent).

Figure 6 shows the time-averaged voltage *vs.* flux for the asymmetric SQUID of figure 3, again with a bias current of 200 μA and shunt resistances of 1 Ω. The junction capacitances are calculated as

above and have values of 1.2 and 0.12 pF, corresponding to critical currents of 100 μA and 10 μA. The calculations show an excellent voltage sinusoid with a voltage modulation of 4 μV relative to an average voltage of about 83 μV, or about 5 percent modulation. A perfect sinusoid is also shown for visual comparison. The frequency spectrum of this SQUID is shown as the crosses in figure 5. The improvement in spectral purity of the asymmetric SQUID over the symmetric SQUID with the same total inductance and critical current is substantial. The second and third harmonics are now down 36 and 69 dB. The depth of modulation
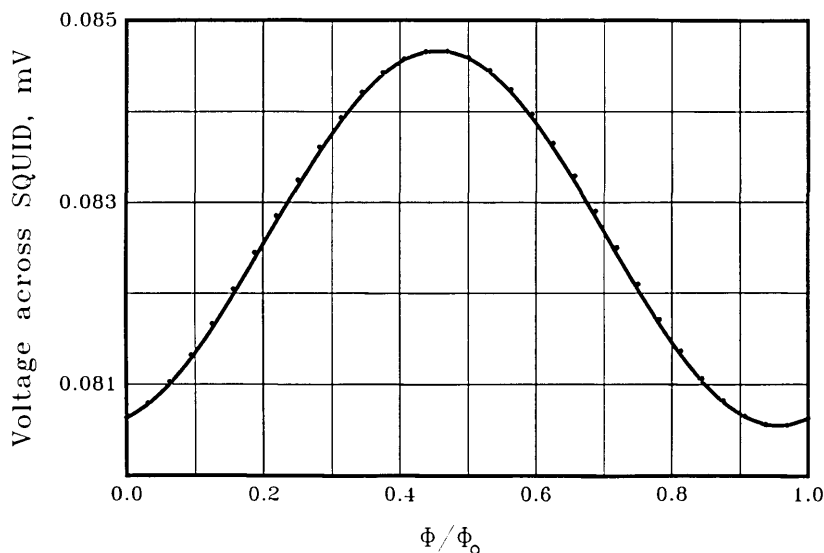
Figure 6—The time-averaged voltage across the asymmetric SQUID of figure 3 with a current bias of 200 μA (dots). Shunt resistances of 1 Ω each are used. Junction capacitances are $C_1 = 1.2$ pF and $C_2 = 0.12$ pF. The solid line is a sinusoid for visual comparison.

of the voltage is not as large as with the symmetric SQUID, however. We find this to be generally true —asymmetric SQUIDs have superior spectral purity but less depth of modulation than symmetric SQUIDs with the same bias current and the same total inductance, critical current, and shunt resistance.

The computed I-V curves of figures 7(a,b) show the differences in modulation for the two SQUIDs considered here. Curves are shown for $\Phi=0$ and $\Phi=0.5\Phi_0$. Note that these values of flux are not quite at the extrema of the voltage for the asymmetric SQUID, as figure 6 shows. Spectral purity generally increases as the bias current is increased, but at the expense of depth of modulation. An exception occurs when an LC resonance significantly affects the current-voltage relation, as shown in figure 8. Here the shunt resistances are kept at 1 Ω but the critical currents, and hence capacitances, of the SQUIDs considered above are doubled, and
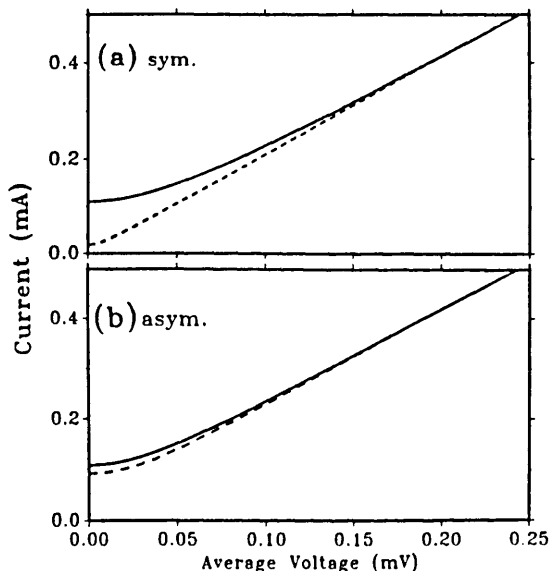
Figure 7—Current-voltage characteristics for dc SQUIDs at $\Phi=0$ (solid curves) and $\Phi=0.5\Phi_0$ (dashed curves). $L_1=L_2=2.0$ pH and $R_1=R_2=1$ Ω for both cases. (a) Symmetric SQUID with $I_{01}=I_{02}=55$ μA, $C_1=C_2=0.66$ pF. (b) Asymmetric SQUID with $I_{01}=100$ μA, $I_{02}=10$ μA, $C_1=1.2$ pF, $C_2=0.12$ pF.
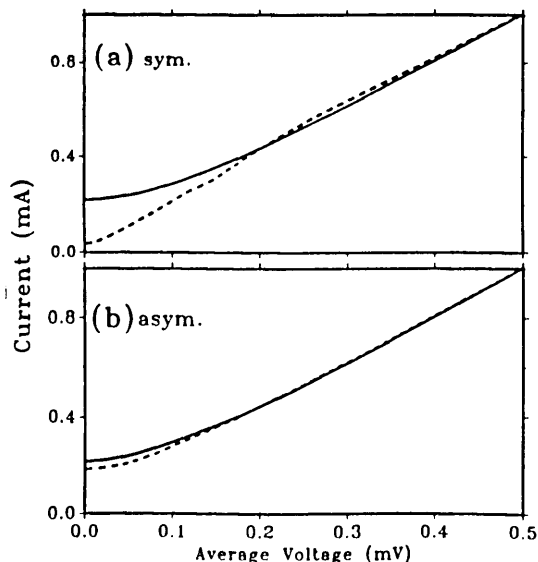
Figure 8—Current-voltage characteristics for dc SQUIDs at $\Phi=0$ (solid curves) and $\Phi=0.5\Phi_0$ (dashed curves). $L_1=L_2=1.0$ pH and $R_1=R_2=1$ Ω for both cases. (a) Symmetric SQUID with $I_{01}=I_{02}=110$ μA, $C_1=C_2=1.32$ pF. (b) Asymmetric SQUID with $I_{01}=200$ μA, $I_{02}=20$ μA, $C_1=2.4$ pF, $C_2=0.24$ pF.

the inductances are halved to keep the LI_c product unchanged. For the symmetric SQUID—figure 8(a)—an LC resonance at $\Phi_0/(2\pi\sqrt{L_1C_1})=0.29$ mV is evident. (The resonance becomes sharper with larger values of shunt resistance.) Calculations for SQUIDs with apparent LC resonances show that the spectral purity of the voltage *vs.* flux curves is degraded. The asymmetric SQUID of figure 8(b) does not show a prominent LC resonance because the two sides of the SQUID interfere; however, the larger capacitance of this example greatly reduces the modulation depth. It is thus important that the junction capacitance be kept as low as possible so that the capacitive impedance does not shunt out the resistance.

Perhaps the principal virtue of the low-inductance SQUIDs, and especially the asymmetric low-inductance SQUIDs, lies in the fact that the harmonics above the second are very greatly reduced and are probably negligible. This is important because the earlier work with rf SQUIDs [5] found that the second harmonic could effectively be nulled, and that the higher harmonics constituted the principal problem. That the second harmonic is also substantially reduced is of course an improvement. Since the basic source of systematic error in the measurement of rf attenuation is caused by harmonic distortion of the sinusoidal response of the system [4], the SQUIDs discussed here should have a distinct advantage over the rf SQUIDs.

In 1982 M. Cromar of this laboratory made a preliminary study on the suitability of a thin-film dc SQUID as the detector element in an rf attenuator-calibrator system (unpublished). Using a resistively shunted symmetric SQUID whose LI_c product was considerably larger than Φ_0, he showed that at low signal frequencies, the zeroes of the response approximated the zeroes of the J_0 Bessel function closely enough that accuracy at rf frequencies comparable to that of the earlier measurements with rf SQUIDs might be realized. This research was not pushed further.

The microfabricated dc SQUIDs are expected to have better thermal and temporal stability than the single-junction rf SQUIDs used earlier. The overall circuitry necessary to attain the output voltage should also be simpler with the dc SQUID. Imperfections in microwave components were found to be a major contributor to the harmonic distortion in the rf SQUID system [5]. Such components would not be used in the readout scheme for a dc SQUID.

The 4-pH inductances used here are small, but SQUIDs with lower inductance have been fabri-

cated. The low inductance of the proposed SQUIDs presents a potential problem of sufficient coupling, however. For example, if the mutual inductance between a 4-pH SQUID and the input line were only 4-pH, about 500 μA would be required in the line to produce one flux quantum in the SQUID. If one desires 200 nulls in the voltage response (100 flux quanta), about 50 mA must flow in the line in this case. Although higher than typical, this value is still below what a superconducting stripline could support. Higher values of mutual inductance will decrease the maximum current needed. The mutual inductance to an input coil carrying the signal can in fact be made much larger than the self-inductance of the SQUID. Planar coupling to low-noise, low-inductance SQUIDs is the subject of much current research [11–13]. Of course, one may also choose to work with higher-inductance SQUIDs, accepting somewhat less spectral purity if the critical currents are kept at the same values, in order to decrease the maximum current needed in the stripline or to decrease the degree of coupling to the SQUID.

The effect of noise is another consideration. It is beyond the scope of this note to undertake a detailed study of noise effects, which depend upon the readout method used. Ideally, of course, it is desirable that the noise of the SQUID plus its readout system be dominated by the intrinsic noise of the SQUID. Readout schemes with this in view are under active investigation; Ketchen [11] discusses several of them. For a readout system operating at a frequency of about 100 kHz, $1/f$ noise is not a consideration. However, even at lower frequencies where $1/f$ noise dominates, a new readout scheme [14] for significantly reducing the noise has been developed.

Properly fabricated dc SQUIDs have the lowest noise figures of any devices [11]. White noise decreases with decreasing inductance, which is favorable for the SQUIDs under consideration. The parameter $2\pi kT/I_0\Phi_0$ is sometimes used to characterize the noise. If we take $I_0=0.11$ mA, which is the average of the critical currents used in the preceding examples, we find the value 0.002 at 4 K for this noise parameter. The ultra-low-noise SQUIDs operate near this value. The spectral density S_V of the voltage fluctuations in a resistor R is given by $4kTR$. For shunt resistances of about 1 Ω, the voltage noise power spectrum is 2×10^{-22} V^2/Hz at 4 K. The flux noise density S_Φ is approximately $S_V/|\partial V/\partial\Phi|^2$. The ultra-low-noise SQUIDs are built to be biased at that value of flux that gives the greatest energy sensitivity, which occurs at the

largest value of $|\partial V/\partial\Phi|$. However, in the present case the flux will be swept over many periods of Φ_0, so that each value of flux contributes almost equally. Since the voltage is nearly sinusoidal, $|\partial V/\partial\Phi|^2$ varies almost as sine-squared, which we may replace by 1/2 times an amplitude, to a good approximation. Thus $S_\Phi \approx 2kTR\,\Phi_0^2/(\pi V_0)^2$, where V_0 is the voltage amplitude. For the symmetric SQUID of figure 4, $V_0 \approx 5.5$ μV so that $S_\Phi \approx 10^{-13}\Phi_0^2/$Hz. These values are not far from values quoted for low-noise SQUIDs [13–15]. Other expressions for the voltage noise power spectrum are available [14,15] which take into account noise contributions from the circulating current in the SQUID. The noise values from these expressions are not significantly different from those calculated above because of the very small inductance. Although these arguments do not establish that noise will not be a significant problem affecting the accuracy of determining the voltage nulls in rf measurements, they show that the SQUIDs proposed here share characteristics of low-noise SQUIDs, and thus are encouraging.

The purpose of this note has been to suggest a new scheme for rf measurements using SQUIDs, and to demonstrate its potential advantages. A more extensive analysis of feasibility could include the following: simulations of the effect of noise upon the accuracy with which the zeroes of the response can be determined; studies of the magnitude and effects of the parasitic inductance associated with the shunt resistors; inclusion of the circuit carrying the signal—source, coupling coil, and load—to determine whether the nonlinear impedance reflected into the circuit by the SQUID is important; determination of the optimum choice of inductance, critical currents, asymmetry, and bias current to obtain the best combination of spectral purity and depth of modulation, or in short the greatest accuracy possible.

The considerations presented here suggest that thin-film, low inductance, low critical current, dc SQUIDs, especially those with asymmetric critical currents, would be superior to rf SQUIDs in rf current, power, or attenuation measurements.

References

[1] Kamper, R. A., and M. B. Simmonds, Broadband superconducting quantum magnetometer, Appl. Phys. Lett. **20** 270–272 (April 1972).

[2] Kamper, R. A.; M. B. Simmonds, C. A. Hoer, and R. T. Adair, Quantum mechanical measurement of rf attenuation, in Proc. Appl. Superconductivity Conf. (IEEE Pub. 72CH0682-5-TABSC) 696–700 (May 1972).

[3] ———, A New Technique for rf Measurements Using Superconductors, Proc. IEEE **61** 121–122 (January 1973).

[4] ———, Measurement of rf Power and Attenuation Using Superconducting Quantum Interference Devices, Natl. Bur. Stand. Tech. Note **643** (August 1973).

[5] Kamper, R. A.; M. B. Simmonds, R. T. Adair, and C. A. Hoer, Advances in the Measurement of rf Power and Attenuation Using SQUIDs, Natl. Bur. Stand. Tech. Note **661** (September 1974).

[6] Petley, B. W.; K. Morris, R. W. Yell, and R. N. Clarke, Moulded microwave SQUID for rf attenuator calibration, Electron Lett. **12** 237–238 (May 1976).

[7] Sullivan, D. B.; R. T. Adair, and N. V. Frederick, rf Instrumentation Based on Superconducting Quantum Interference, Proc. IEEE **66** 454–463 (April 1978).

[8] Peterson, R. L., and D. G. McDonald, Voltage and current expressions for a two-junction superconducting interferometer, J. Appl. Phys. **54** 992–996 (February 1983).

[9] Peterson, R. L., and C. A. Hamilton, Analysis of threshold curves for superconducting interferometers, J. Appl. Phys. **50** 8135–8142 (December 1979).

[10] Fulton, T. A.; L. N. Dunkleberger, and R. C. Dynes, Quantum interference properties of double Josephson junctions, Phys. Rev. **B6** 855–875 (August 1972).

[11] Ketchen, M. B., dc SQUIDs 1980: The state of the art, IEEE Trans. Magn. **MAG-17** 387–394 (January 1981).

[12] Jaycox, J. M., and M. B. Ketchen, Planar coupling scheme for ultra low noise dc SQUIDs, IEEE Trans. Magn. **MAG-17** 400–403 (January 1981).

[13] Cromar, M. W., and P. Carelli, Low-noise tunnel junction dc SQUIDs, Appl. Phys. Lett. **38(9)** 723–725 (May 1981).

[14] Foglietti, V.; W. J. Gallagher, M. B. Ketchen, A. W. Kleinsasser, R. H. Koch, S. I. Raider, and R. L. Sandstrom, Low frequency noise in low-1/f-noise dc SQUIDs, Appl. Phys. Lett. (in press).

[15] Voss, R. F.; R. B. Laibowitz, A. N. Broers, S. I. Raider, C. M. Knoedler, and J. M. Viggiano, Ultra low noise Nb dc SQUIDs, IEEE Trans. Magn. **MAG-17** 395–399 (January 1981).

Catalytic Cracking
As the Basis for a Potential Detector
For Gas Chromatography

Thomas J. Bruno

National Bureau of Standards
Boulder, CO 80303

This short paper describes the design, construction and preliminary experimental results obtained with a potential new detector for the gas chromatographic analysis of hydrocarbon species. The functional principle of the detector is the measurement of the temperature change of a catalyst as catalytic cracking occurs on its surface. The catalyst is a silicon dioxide-aluminum oxide-zeolite mixture similar to the materials used commercially in industrial riser crackers. The temperature drop which occurs at the onset of cracking is measured using two opposed thermocouple junctions.

The first prototype, described in this paper, consists of a single pair of junctions. After appropriate signal conditioning (using a commercially available filter-amplifier), the thermocouple output is logged using an electronic integrator. Work on multi-junction cells, which is currently in progress, is also described briefly.

Key words: catalytic cracking; detector; gas chromatography.

Accepted: February 18, 1987

Introduction

The detection of the separated components from a gas chromatographic column is usually based upon the measurement of some property of the analyte species which is easily and clearly distinguishable from that of the carrier gas [1,2].[1] Included among the many detectors developed for gas chromatography have been several that are based upon the analyte undergoing a catalyzed reaction [3–8]. In most of these approaches, catalysis results in the production of reaction products to which conventional gas chromatographic detectors are more sensitive, or in the production of an ion current which is measured using a very sensitive electrometer.

Thus, in most of these detectors, the chemistry occurring during the catalyzed reaction and the nature of the catalyst itself are of secondary importance. This short note is a report of preliminary work on a potential detector which senses the temperature change of a cracking catalyst during reactions with appropriate hydrocarbon species.

Catalytic cracking has been of immense industrial importance since its introduction in 1927 [9]. The development of the technology of catalytic cracking has resulted in 10 commercial processes available for license. Because of the pressures of the marketplace, much of the science behind this mature technology remains buried in the vaults of proprietary secrecy. The catalytic cracking process is known to proceed through a carbonium ion mechanism [10]. This is to be contrasted with thermal cracking, which occurs via a free radical mechanism. Catalytic cracking is an endothermic process which requires a net input of heat to be

---

[1]Figures in brackets indicate literature references.

applied to the system [11]. The major products of the catalytic cracking of normal hydrocarbons (up to n-hexadecane) are C_3 to C_6 branched hydrocarbons. Cracking catalysts have virtually no effect on low molecular weight hydrocarbons such as propane or n-butane. The ease of cracking usually increases with the hydrocarbon molecular weight. Among aliphatic hydrocarbons, cracking is accelerated by tertiary groupings, but is retarded by quarternary groupings (for example, that found in 2,2-dimethylbutane). Thus, a molecule may possess functionalities that have competing effects toward the cracking process [12].

Catalysts for cracking are usually formulated from a silica-alumina mixture which contains 10 to 20 percent aluminum oxide. Recently, the addition of up to 15 percent synthetic sodium alumino-silicate (type X zeolite molecular sieve) has provided greater catalytic activity. Commercial catalysts often have trace quantities of rare earth metals or platinum, but this is mainly done to assist in the process of hydrocracking (cracking followed by hydrogenation).

Experimental

The two modifications of the prototype catalytic cracker detector which have been tested to demonstrate the potential of the approach are depicted in figures 1 and 2. The detectors are similar in concept to the adsorption detectors which have been designed for liquid chromatography [13] and supercritical fluid chromatography [14]. Each detector consists of two K-type (chromel-alumel) thermocouple junctions. One of the junctions is coated with catalyst, while the other serves as a reference. The catalyst employed was a mixture of 70 percent silicon dioxide, 20 percent aluminum oxide, and 10 percent sodium alumino-silicate (13-X type molecular sieve). The source of silicon dioxide was a high thermal conductivity silica based ceramic adhesive which contains a small percentage of binders. A thin layer of the mixture (suspended in water) was coated on the twisted strands of each sensing junction. The junctions were then mounted within the detector chamber (made from 316 stainless steel) using a zirconia-based gas-tight ceramic adhesive. In the first modification (fig. 1), the reference junction is mounted directly inside of the detector chamber, downstream from the sensing junction. In the second modification, the reference junction is mounted external to the detector chamber, potted in the zirconia ceramic adhesive mentioned earlier. In each case, the assembled detector cell is mounted inside of a copper block (to integrate out temperature variations) which is then placed inside of a small muffle furnace. The muffle
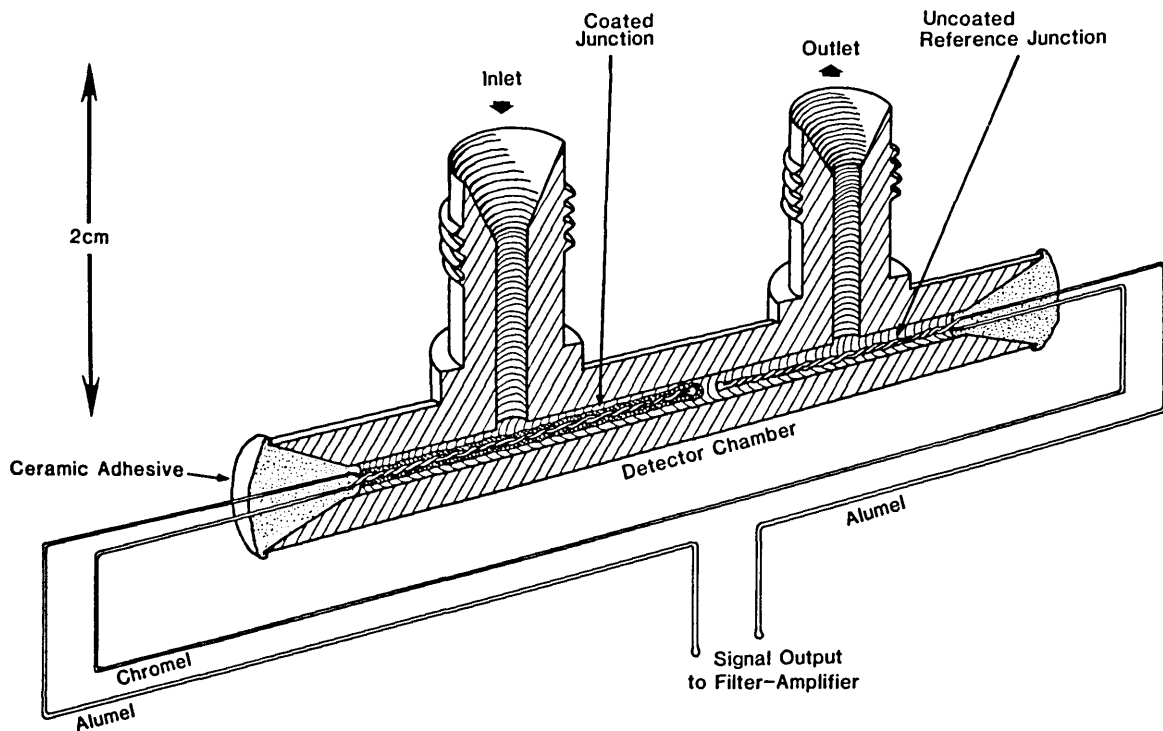
Figure 1-Catalytic cracker detector having the reference junction in the gas stream.
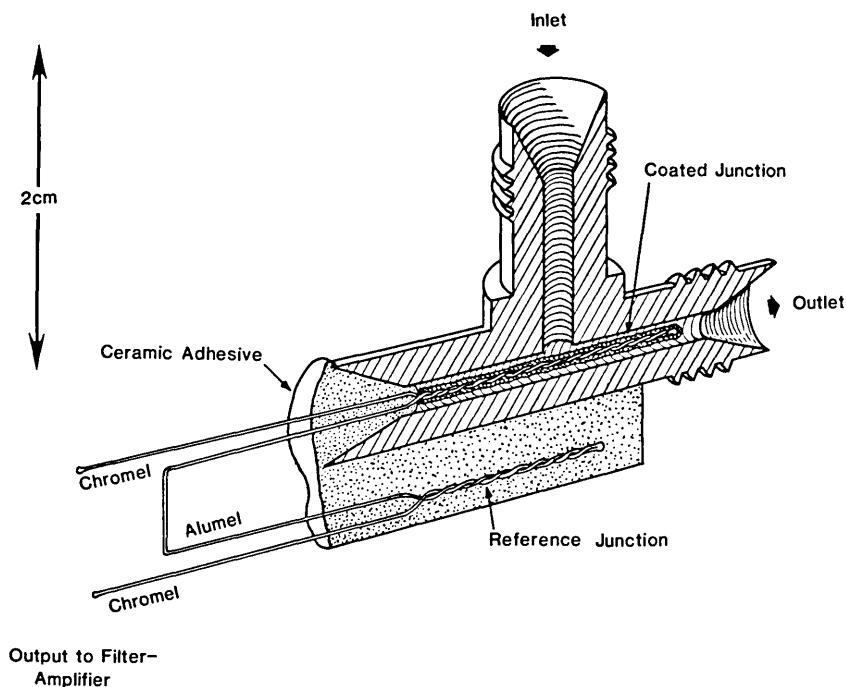
Figure 2-Catalytic cracker detector having the reference junction mounted remotely from the gas stream.

furnace is positioned next to the column outlet of a commercial gas chromatograph. The inlet port of the detector is preceded by approximately 25 cm of stainless steel tubing (0.16 cm o.d., 0.03 cm i.d., not shown in the figures). This length of tubing serves as a heat exchanger (inside the muffle furnace) to preheat the carrier gas and analyte before they enter the detector cell. This heat exchanger is approximately 10 times the length necessary to provide 99 percent temperature equilibration. In subsequent modifications of this detector, the heat exchanger length will be optimized, and the transfer line length (from the column) will be minimized. The detector cell and heat exchanger tube are maintained at 550 °C during operation. This is the temperature at which catalytic cracking is optimum in commercial riser crackers using the silica-alumina-zeolite catalyst mixture.

As mentioned earlier, the functioning of the prototype catalytic cracker detector is based upon the measurement of the decrease in temperature of the coated junction (upon contact with a crackable hydrocarbon) with respect to the uncoated (fig. 1) or remote (fig. 2) reference junctions. Type K thermocouples provide a potential difference of 43 μV/deg in the temperature range of interest [17]. The output of the thermocouples is fed into a commercial filter-amplifier designed for chromatographic applications. The output of this device is then sent on to a commercial electronic integrator.

The filter-amplifier was used with a gain setting of 1, and only served to decrease short term noise. It is, in fact, possible to eliminate this device altogether and feed the detector signal directly to the integrator. Chromatograms which are quite acceptable may be obtained in this fashion.

Preliminary Results

A sample chromatogram showing the detector response to 5μl of a mixture of n-hexane and n-octane (60/40 approximate mole percent) is shown in figure 3. This chromatogram was obtained using the detector depicted in figure 1. The separation was performed on a 3 m packed column of Porapak-QS [1],[2] at a column temperature of 200 °C, using helium (at a flow-rate of 30 mL/min) as the carrier gas. The integrator-recorder was programmed for a full-scale sensitivity of 8 μV. Thus, the peaks obtained correspond to a catalyst temperature drop of between 0.12 °C and 0.16 °C. The response of the detector is selective for crackable hydrocarbons. Thus, samples of n-butane and

[2]Certain commercial equipment, instruments, or materials are identified in this paper in order to adequately specify the experimental procedure. Such identification does not imply recommendation or endorsement by the National Bureau of Standards, nor does it imply that the materials or equipment identified are necessarily the best available for the purpose.
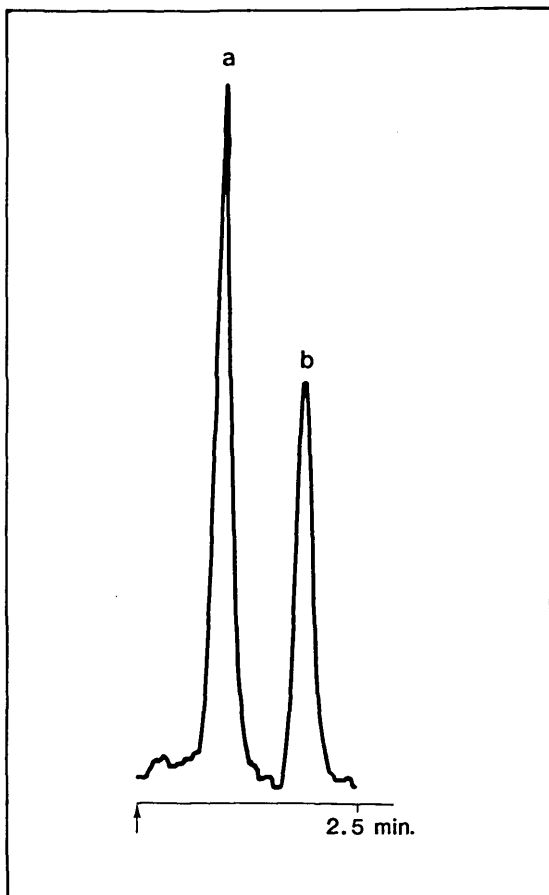
Figure 3–Chromatogram showing the response of the detector to n-hexane (a) and n-octane (b).

propane were unresponsive, as was a mixture of freons. The detector responds also to alkyl substituted aromatic hydrocarbons, with the response increasing with the size of alkyl substituent. This observation is expected in view of the work by Haensel [10]. Benzene gives an erratic response, since at elevated temperatures (and in contact with stainless steels) the preferred reaction is the formation of biphenyl [18,19].

After several weeks of operation, a deposit of coke was found to have formed upon the surface of the coated junctions. This is expected, since coke formation always occurs in commercial riser crackers. The coke layer did not cause a noticeable decrease in the activity of the detector, probably because of the relatively small quantity of hydrocarbon undergoing reaction in the detector relative to that commercial situations. The coke layer is easily burned off in the presence of air.

Conclusions

The preliminary work on the catalytic cracker detector shows that the device has a good deal of potential as the basis of a detector for the selective analysis of hydrocarbons. It does not require a continuous stream of carrier gas, as does a thermal conductivity detector (TCD), nor does it require the fuel and oxidant of a flame ionization detector (FID). The circuitry required for the detector is extremely simple, consisting of a low-cost filter amplifier instead of the bridge circuit (for the TCD) or the electrometer (for the FID). These features make the catalytic cracker detector attractive for continuous line process analysis in an industrial environment, where safety, durability and simplicity is of paramount concern.

In its present form, the prototype detector has some major drawbacks. The first and most important is the low sensitivity (approximately three orders of magnitude lower than the TCD). We are addressing this problem by constructing multiple-junction thermopile cells in order to boost the signal level. Results with a six-junction cell have been very encouraging, with a nearly five-fold increase in sensitivity being observed. The six-junction prototype is similar in concept to that shown in figure 1. It is clear that very significant increases in sensitivity are possible with multiple junction cells. We are currently constructing a 12-junction thermopile cell which incorporates a flow-through catalyst design. Measurement of sensitivity and linear dynamic range, as well as testing the effects of different carrier gases and flow-rates, will be performed on this model. Current work on the multi-junction cells is done using a commercially available proportional SCR temperature controller instead of the muffle furnace. This device provides far better temperature control and uses only 10 percent as much power as the muffle furnace.

References

[1] David, D. J., Gas Chromatographic Detectors, John Wiley and Sons: New York (1974).
[2] Sevčík, J., Detectors in Gas Chromatography, Elsevier Scientific Publishing Co.: Amsterdam (1976).
[3] Umstead, M. E.; F. J. Woods and J. E. Johnson, J. Chromatogr. Sci., 8 375 (1970).
[4] Nyarady, S. A.; R. M. Barkley and R. E. Sievers, Anal. Chem., 57 2074 (1985).
[5] Wells, G., Anal. Chem., 55 2112 (1983).
[6] Sutton, D. G.; K. R. Westberg and J. E. Melzer, Anal. Chem. 51 1399 (1979).

[7] Rosset, R.; M. Caude, J. C. Escalier, and C. Bollet, J. Chromatogr., **167** 125 (1978).

[8] Davis, B., Anal. Chem., **49** 832 (1977).

[9] Gary, J. H., and G. E. Handwerk, *Petroleum Refining Technology and Economics*, 2nd Ed., Marcel Dekker Inc.: New York (1984).

[10] Haensel, V., Adv. in Catalysis, **3** 179 (1951).

[11] Scatterfield, C. N., *Heterogeneous Catalysis in Practice*, McGraw Hill: New York (1981).

[12] Good, G. M.; H. H. Voge and B. S. Greensfelder, Ind. Eng. Chem., **39** 1032 (1947).

[13] Hupe, K.-P., and E. Bayer, J. Gas Chromatogr. **5** 197 (1967).

[14] Cashaw, J. L.; R. Segura and A. Zlatkis, J. Chromatogr. Sci., **8** 363 (1970).

[15] Mark, H. F.; D. F. Othmer, C. G. Overberger, and G. T. Seaborg, eds., *Kirk-Othmer Encyclopedia of Chemical Technology*, 3rd. ed., Vol. 5, John Wiley and Sons: New York (1979).

[16] Breck, D. W., *Zeolite Molecular Sieves*, John Wiley and Sons: New York (1973).

[17] Powell, R. L.; W. J. Hall, C. H. Hyink, and L. L. Sparks, *Thermocouple Reference Tables Based on the IPTS-68*, NBS Monograph 125, National Bureau of Standards, Washington, DC (1974).

[18] Hancock, E. K., ed., *Benzene and its Industrial Derivatives*, John Wiley and Sons (Halsted Press): New York (1975).

[19] Straty, G. C.; M. Ball and T. J. Bruno, J. Chem. and Eng. Data, in press.

A Finite Element Study Of Transient Wave Propagation in Plates

Mary Sansalone, Nicholas J. Carino, Nelson N. Hsu

National Bureau of Standards
Gaithersburg, MD 20899

Studies of transient wave propagation in plates were carried out to establish a basis for the impact-echo technique as a nondestructive test for flaw detection in concrete. The surface displacements caused by stress waves generated by point impact on a plate were calculated using both the Green's function solution and the finite element method; displacement waveforms obtained by the two approaches showed good agreement. Displacement and stress fields in a plate were studied using finite element analysis. It was shown that transient point load applied normal to a stress-free boundary gives rise to P- and S-"wakes"—disturbances trailing the P- and S-waves. The displacement and stress fields in each wake resemble those in the preceding wave.

Key words: finite element analysis; Green's function; impact; impact-echo method; plate response; stress wave propagation.

Introduction

For more than 30 years, efforts have been made to apply stress wave propagation to nondestructive testing of concrete. These efforts have met with limited success, although some progress has been made in measuring the thickness of plate elements and for integrity testing of rod-like structures, such as piles [1][1]. Progress has been limited because of the heterogeneous nature of concrete, which strongly attenuates high frequency waves; thus traditional wave propagation methods developed for flaw detection in metals cannot be used for evaluation of concrete.

The National Bureau of Standards has been working to develop a nondestructive test method for concrete using transient stress waves [2-4]. This method is referred to as the impact-echo method. The technique involves introducing a transient stress pulse into a test object by mechanical impact at a point and monitoring reflections of the pulse from internal defects and external boundaries. Stress pulses with sufficient energy have been generated by dropping small diameter (4–16 mm) steel spheres (ball bearings) onto concrete.

The impact-echo test is a simple procedure; however, successful interpretation of displacement waveforms requires an understanding of the interaction of transient stress waves with internal defects. The current state of knowledge about the propagation of transient stress waves in bounded

---

About the Authors: Mary Sansalone and Nicholas J. Carino serve with the Center for Building Technology, and Nelson N. Hsu is with the Center for Manufacturing Engineering. The two centers are part of the National Engineering Laboratory at NBS.

---

[1]Figures in brackets indicate literature references.

solids containing defects is very limited. Thus the NBS program has focused on understanding the nature of transient stress wave propagation in solids containing defects as well as on the implementation of the impact-echo method. In a current phase of the program, the finite element method is being used to study displacement and stress fields generated by point impact on an elastic solid and the interaction of transient waves with internal discontinuities and stress-free boundaries.

This paper presents results of finite element analysis of transient stress wave propagation in plates. To verify the analyses, surface displacement time histories obtained from the finite element method are compared to exact Green's function solutions for impact on an infinite plate. A second paper, also appearing in this issue of the *Journal of Research*, presents a finite element study of the diffraction of transient waves by planar flaws in a plate.

Background
Transient Wave Propagation

Point impact on the surface of a solid gives rise to three types of transient disturbances: dilatational and distortional waves which propagate into the solid along spherical fronts, and a Rayleigh (R) wave which propagates along a circular front over the surface of the solid. The dilatational and distortional waves are commonly referred to as P- and S-waves. In addition, there is a low amplitude wave known as a head wave. The front of the head wave extends from the intersection of the P-wavefront with the surface of the solid to a point that is tangent to the S-wavefront. Figure 1 is a schematic representation of the P-, S-, R- and head wavefronts generated by a point impact on an elastic solid.

P- and S-waves are characterized by the direction of particle motion with respect to the direction the wavefront is propagating. In the P-wave, displacement is parallel to the direction of propagation; in the S-wave, the motion is perpendicular to the direction of propagation. These waves travel at different speeds; their relative speeds depend on the Poisson's ratio of the material being tested. For a Poisson's ratio of 0.2, which is a typical value for concrete, the S- and R-waves travel at approximately 61% and 56% of the P-wave speed, respectively [1].

The P- and S-waves are reflected by stress-free boundaries and by internal defects of sufficient size. For example, in a plate, multiple reflections occur as the waves travel back and forth between the two free surfaces. This type of reflection is referred to as specular reflection. When a P-wave strikes a boundary at an oblique angle, an S-wave can also be produced by the process of mode-conversion. Likewise, an incident S-wave produces a P-wave. The angles of specularly reflected and mode-converted waves are determined by Snell's Law [5]. A receiving transducer located on the top surface of the plate, near the point of impact, responds to the surface displacements caused by the successive arrivals of each reflection from the bottom of the plate.

Due to the complexity of the problem, explicit equations for the radiation pattern produced by a transient point source on a semi-infinite solid have not yet been derived. Ideas about the nature of this radiation pattern come from knowledge about a
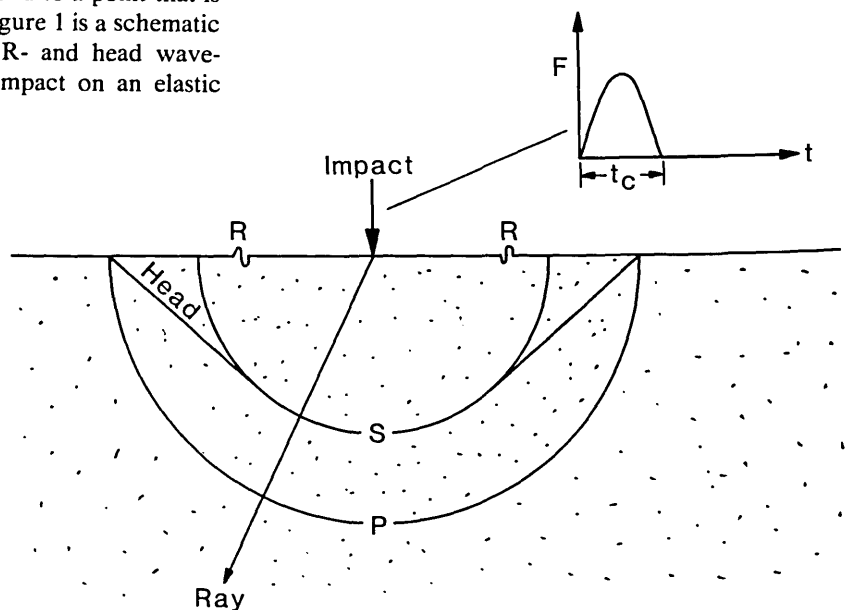
Figure 1-Schematic representation of the wavefronts produced by point impact on a semi-infinite solid.

harmonic point source on a semi-infinite solid [6–8]. Figure 2 shows the angular variation of the amplitude of displacements within the P- and S-waves for a material with Poisson's ratio equal to 0.2. In the P-wave, the amplitude of the displacements is maximum at the centerline of the plate and decreases to zero at the surface. In the S-wave, the amplitude of displacements is zero at the centerline of the plate and at the surface and is maximum along a ray located approximately 40 degrees from the centerline. There is a discontinuity in the S-wave displacements at an angle, θ_c, given by the following equation:

$$\theta_c = \arcsin\left(C_s/C_p\right) \qquad (1)$$

where C_s = S-wave speed, m/s; and
 C_p = P-wave speed, m/s.

In this paper, the finite element method is used to study the nature of the internal displacement and stress fields produced by a transient point load on a plate.

Green's Function Solutions

Theoretical solutions for transient wave propagation in solids are available for a limited number of problems; these solutions can be used to obtain the displacement response at points in a solid. The displacement, $u(r,t)$, at a point due to an impact at some other point on an elastic body can be represented by a convolution integral:

$$u(r,t) = \int_0^t G(r, t-\tau) F(\tau) d\tau \qquad (2)$$

where $F(t)$ is the impact force as a function of time and G (r,t) is the dynamic Green's function of the elastic body. The Green's function is defined as the impulse (dirac delta function) response of the body for a particular impact configuration (impact at one location and the receiver at a different location).

The Green's function solution is the exact solution to the partial differential equations and associated boundary conditions governing elastic wave propagation. Green's function solutions can be obtained using Generalized Ray Theory[2]. The solution is in the form of an infinite series expansion. Stress waves can be visualized as propagating along ray paths. Each term in the series corresponds to the arrival of successive stress waves which propagate along the various ray paths that connect the impact source to the receiver. For a given time duration, a finite number of rays (terms in the series expansion) contribute to the total displacement response at the receiver.

Explicit formulae for Green's function solutions which are amenable to numerical computations have been derived only for simple geometries, such

---

[2] Generalized Ray Theory was originally developed in the 1960's for geophysical applications, but is readily applicable to the study of transient waves in bounded solids. For an introduction to the ideas and formulation of ray theory, see ref. [9].
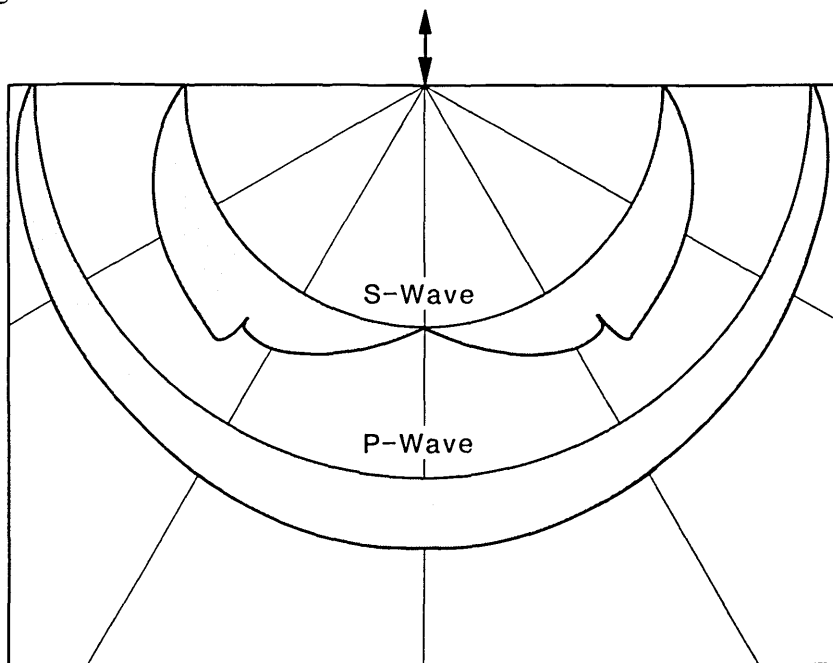
Figure 2–Amplitude of particle displacements in the radiation pattern produced by a harmonic point source.

as a semi-infinite space or an infinite plate. (For computation of the Green's function, see refs. [10,11]. To obtain displacement and stress fields in bounded solids, the finite element method was used.

Finite Element Method

The finite element method is a general numerical technique for obtaining approximate solutions to the partial differential equations that arise from boundary value problems. The method involves dividing a continuum into a finite number of discrete parts—the finite elements. The discretized representation of the continuum is referred to as the finite element model. For stress analysis, the behavior of each element is described by a set of assumed functions which represent the variation of displacements or stresses within that element. Variational (or energy) principles are used to formulate force-displacement element equations. These element equations are then used to construct the global equations which describe the behavior of the entire continuum. Solution of these global equations gives the displacements or stresses at points in the element [12].

An explicit, two-dimensional (axisymmetric or plane strain), finite element code (DYNA2D), developed at Lawrence Livermore Laboratory for solving finite-deformation, dynamic contact-impact problems [13–15], was used to perform the studies discussed in this paper. An input generator (MAZE) [16] was used to create the finite element model. A mini-computer with a virtual operating system, 8 MBytes of memory, and a floating point processor were used to carry out the analyses.

IN DYNA2D, a continuum is divided into elements using constant strain (linear displacement) triangles and quadrilaterals [13]. Higher order elements (e.g., linear strain, quadratic strain) are not available in DYNA2D because they are computationally expensive in wave propagation applications relative to the constant strain elements. For a particular element type, the accuracy of the finite element solution is partly determined by element size. In wave propagation problems, the optimum element size depends on the geometry of the continuum and on the time-history of the dynamic loading. For the constant strain quadrilaterals and the dynamic loading functions used in the linear elastic, plate analyses presented in this paper, convergence studies were carried out to determine the optimum element size. The criteria for convergence were comparisons made between finite element displacement time-histories obtained at points

on the top and bottom surfaces of a plate and the waveforms obtained at the same points by the Green's function solution for an infinite plate. For 0.25 m to 0.5 m thick plates subjected to a force-time function which simulated impact by a steel sphere (contact time of impact was 25 to 31 μs), rectangular elements with dimensions on the order of 0.02 times the plate thickness were found to give sufficiently accurate results. The elastic material properties used in these analyses were representative of concrete.

In dynamic finite element analyses, numerical integration of the equations of motion must be carried out; DYNA2D uses the central difference method [13] to perform this integration. The central difference method requires a small time step for numerical stability. This is not a drawback because wave propagation applications require the use of very small time steps to obtain an accurate solution. Numerical stability requires that the time step, h, meet the following criterion:

$$h \leqslant h_{max} = L/C_p \qquad (3)$$

where L = shortest dimension of the
        element, m; and
    C_p = P-wave speed in the material, m/s.

In DYNA2D, the time step is taken as $0.67h_{max}$ unless the user specifies some other value. During an analysis, data are stored in data files at intervals specified by the user. In the analyses discussed in this paper, data were stored every 2 μs. An interactive graphic post-processor (ORION) [17] was used to process the results of the analyses.

Before the finite element code could be used with confidence to study transient wave propagation in bounded solids containing internal flaws, solutions obtained from the finite element analyses were verified using the Green's function solutions for infinite plates.

Plate Response

The successful implementation of the impact-echo technique as a method for flaw detection in heterogeneous materials, such as concrete, requires an understanding of the reflection of transient stress waves by the free boundaries of a solid and the interaction of waves with internal defects. A first step is understanding the response of an infinite, homogeneous plate to impact. In the following discussion of the elastic response of a plate to point impact on the top surface, the following ana-

lytical results are presented: 1) the displacement time-history obtained at the bottom surface of the plate directly under the impact point; 2) displacement fields recorded at successive times to show transient stress waves propagating within the plate; and 3) the displacement time-history of a point on the top surface of the plate near the point of impact.

For the case of a sphere impacting on a plate, eq (2) can be used to predict the surface displacement that will be detected by a receiving transducer located on either the top or bottom surface of the plate. Two test configurations are considered in this study; these are shown in figure 3. Figure 3(a) shows the receiver located at the epicenter, that is, on the bottom surface of the plate directly under the point of impact. Figure 3(b) shows the impact-echo configuration—the receiver is located on the top surface of the plate near the point of impact. For this configuration, the separation between impact point and receiver is denoted by an H.

The time-history of the contact force generated by the elastic impact of a sphere dropped on the surface of a plate can be approximated by a half-cycle sine curve (see fig. 1). The contact time of the impact and the maximum contact force can be computed if the size and elastic properties of the sphere, the velocity of the sphere at impact, and the elastic properties of the plate are known [18]. If the appropriate Green's function, $G(r,t)$, is also known, then the displacement, $u(r,t)$, can be computed by numerical solution of the convolution integral given by eq (2) [19].
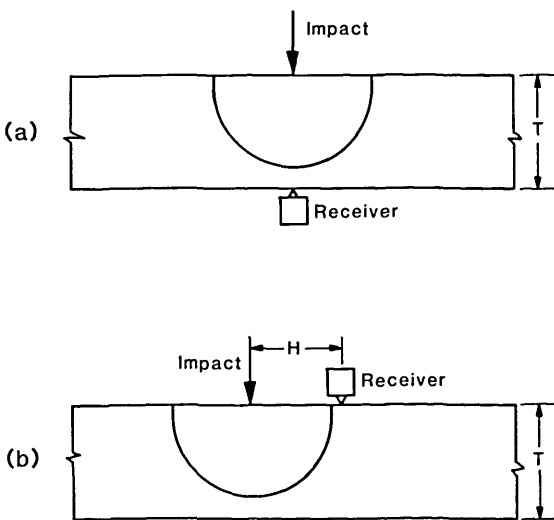
Figure 3–Test configurations for a plate: (a) epicenter; and (b) impact-echo.

In this study, the Green's function for an infinite plate was obtained using a computer code recently developed at NBS [20,21]. This program computes the response for a unit step force-time function input. To obtain the Green's function (impulse response), the derivative with respect to time of the step function solution is calculated. The step function response is calculated using nondimensionalized variables so that the solutions are applicable to a plate of any thickness. Values of the step function response are calculated at prescribed time steps so that the computer solution is a discretized representation of the true solution. The only input parameters required are the source-receiver geometry and the ratio of S- to P-wave speeds. In the analyses presented in this paper, the ratio was 0.61 (Poisson's ratio equal to 0.2).

Epicenter Response

Green's Function Solution: Before considering the response of a plate to impact by a sphere, the impulse response is shown. In the impulse response, wave arrivals correspond to abrupt discontinuities in the waveform. It is therefore easier to determine the displacements caused by each individual wave arrival.

Since the numerical solution used in this study results in a discrete representation of the step function response, the derivative of this solution (the impulse response) also has a discrete representation.

The impulse response for a 0.25 m thick plate is shown in figure 4. The P- and S-wave speeds are 4000 and 2440 m/s, respectively. A time step of 1 μs was used in the calculations. This response consists of normal surface displacements caused by the arrival of direct P- and S-waves, multiply reflected waves (3P, 3S, 5P, etc.) and mode-converted waves (2PS, P2S, etc.). The arrival times of these waves are indicated on the waveform.

The P-wave generated by impact on the top surface of the plate is the first wave to arrive at the epicenter; it is a compression wave (a wave causing compressive stress at the wavefront) and it causes a large downward displacement of the surface. This compression wave will be reflected at the bottom surface of the plate as a tension wave. The tension wave will propagate back up through the plate to be reflected at the top surface as a compression wave. (The multiply-reflected P-wave is now called the 3P-wave because when it arrives at the bottom of the plate it will have traveled through the thickness of the plate three times.) When the 3P-wave arrives at the bottom surface it pushes the

EPICENTER SOLUTION
DELTA FUNCTION INPUT (0.25 M)
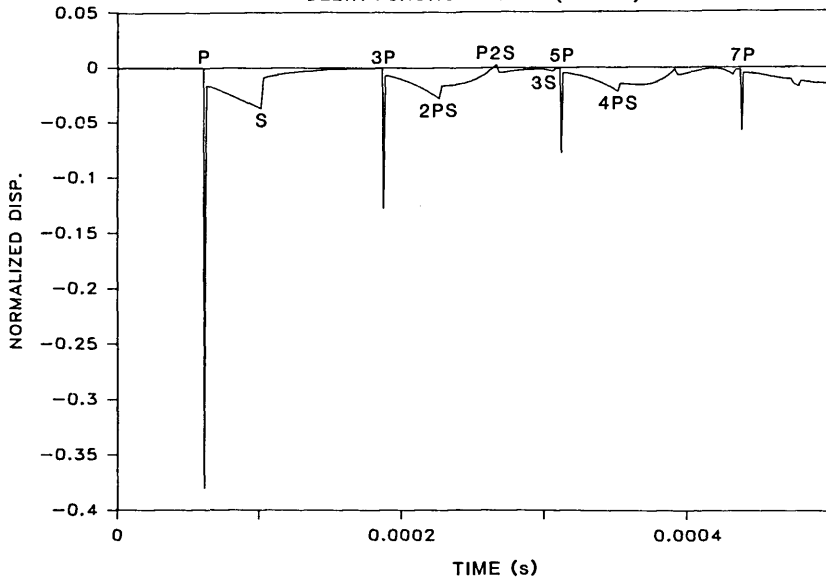
Figure 4-Epicenter response to a delta function impact.

surface downward. This cycle is repeated so that every multiply-reflected P-wave arriving at the bottom surface of the plate (5P, 7P, etc.) is a compression wave that causes a downward displacement of the plate surface.

Notice that the amplitude of the surface displacements caused by successive P-wave arrivals decreases. This is due to divergence (spherical beam spreading) which causes the amplitude of the displacement to decrease as the inverse of the distance the wave has traveled [22].

Theoretically, an S-wave arriving at the epicenter has no vertical displacement component (see fig. 2). However, the arrival of the S-wavefront is still easy to identify because the arrival of the wavefront corresponds to a discontinuity in the vertical displacement at the epicenter.

The waveform obtained from the Green's function solution for a point located a distance r from an impulse point source in an infinite solid shows displacements corresponding to the arrival of the P- and S-wavefronts. No other displacements occur. However, in the impulse response of the infinite plate (fig. 4), notice that in addition to the displacements caused by P-, S-, and mode-converted waves, there are displacements that occur between the arrivals of each of these waves. These intermediate displacements are referred to in this paper as "wakes"; they result from the transient point source being applied normal to a stress-free boundary and from the interaction of propagating waves with the lower stress-free boundary of the plate. In the frequency domain these wakes are

commonly thought of as geometric dispersion phenomena.

To obtain the epicenter response caused by a sphere impacting the top surface of the plate, the waveform shown in figure 4 must be convolved with the force-time function shown in figure 1. Using the identity for the derivative of convolution, a mathematically equivalent approach, which is numerically more accurate in this case, is to convolve the response function, $H(r,t)$, computed for a unit step function with the derivative of the force-time function, $dF(t)/dt$ [19]. Thus, eq (2) can be written in the following form:

$$u(r,t) = \int_0^t H(r,t-\tau) \frac{dF(\tau)}{dt} d\tau \qquad (4)$$

In this case, the derivative of the force-time function is a half-cycle cosine curve. The waveform obtained by this convolution is shown in figure 5(a). The time step used in these calculations was 2 μs.

In this analysis, the contact time of the impact was 31 μs, which is equal to one-half the time required for a P-wave to travel from the impact point to the epicenter. The waveform generated by a 31 μs point impact is much smoother than the impulse response that was shown in figure 4. As the contact time increases, wave arrival times can become difficult to determine as displacements caused by individual waves become smeared together. As a result, sudden changes in the waveform will not necessarily correspond to the arrival times of the

waves. (See refs. [3,4] for a more detailed discussion of the effect of contact time on surface displacement waveforms.)

The arrivals of P-, S-, and mode-converted wavefronts are indicated on the calculated waveform. The displacements caused by the large amplitude P-wave arrivals dominate the waveform. Notice that there is a second dip in the waveform after the end of the direct P-wave and before the arrival of the S-wavefront. The steady change in displacement (wake) between these two waves in the impulse response (see fig. 4) gives rise to this second dip.

Comparison With Finite Element Solution: The impact response of the same plate was also calculated using an axisymmetric finite element model. In both the Green's function solution and the finite element analysis the plate was unsupported. Impact on the top surface of the plate was simulated by applying a uniform stress over an element at the center of the plate. The time history of the applied stress was a half-cycle sine curve with a duration of 31 μs. The values of the material properties used in the analysis were: a modulus of elasticity of 33100 MPa, a Poisson's ratio of 0.2, and a density of 2300 kg/m^3. These values result in P-, S-, and R-wave speeds of 4000, 2440, and 2240 m/s, respectively. Figure 5(b) shows the normal displacement at the epicenter of the plate. The computed arrival times of P-, S-, and the mode-converted PS-wave are indicated on the waveform.

The response obtained by the finite element analysis can be compared with the Green's function solution for an infinite plate for the period of time before wave reflections return from the sides of the bounded plate used in the finite element analysis. If the shape and magnitude of the perturbations in the waveform obtained from the Green's function solution [fig. 5(a)] are compared with those obtained from the finite element analysis [fig. 5(b)], it is seen that there is good agreement between the two waveforms.

In the waveform obtained from the finite element analysis, there is a series of low amplitude, extraneous oscillations (ringing) between 128 μs and the arrival of the 3P-wavefront. This ringing is due to the excitation of spurious modes of vibration in the constant strain finite elements used in DYNA2D. These modes are referred to as "zero energy" or "hourglass modes" [14] and they are due to distortions of the elements. A decrease in the contact time of the impact causes more rapid changes in displacement; this causes distortion of elements and tends to increase ringing. Artificial
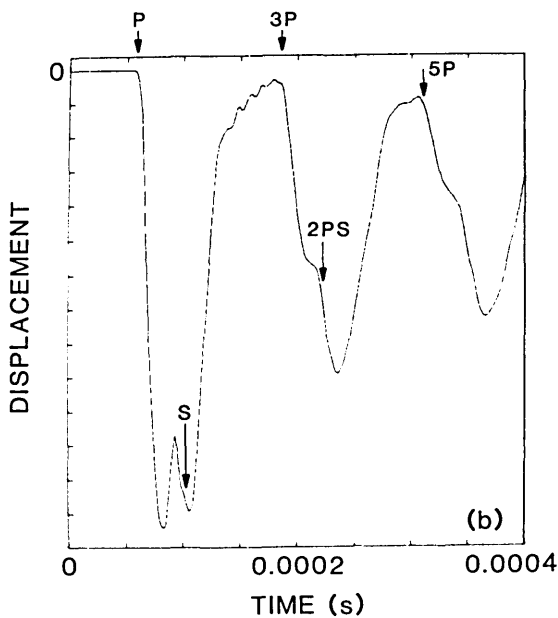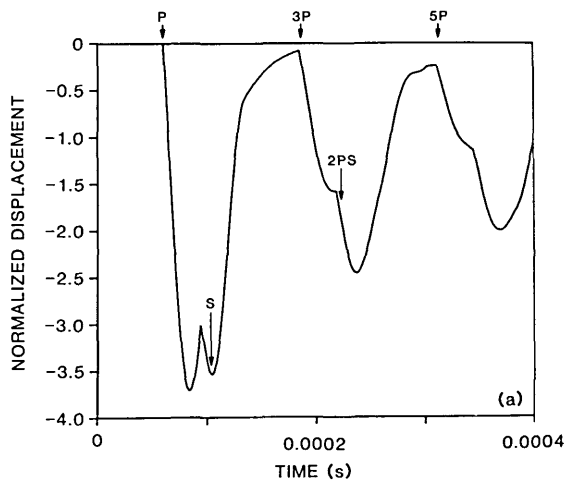
Figure 5–Epicenter response to impact: (a) Green's function solution; and (b) waveform obtained from finite element analysis.

viscosities are introduced in DYNA2D to damp out the ringing [23], but it generally cannot be completely suppressed. The ringing is particularly evident in this case because there is a relatively quiescent period between the rapid change in displacements which occurs prior to 128 μs and the arrival of the 3P-wave.

Displacement Fields Within a Plate

A single finite element analysis solves for displacements and stresses over the entire domain (the

collection of finite elements) at each time step during the specified time of analysis. These results can be used to study the dynamic displacement and stress fields that are produced within a solid.

An axisymmetric, finite element analysis was performed for a 25 μs duration impact on a 0.5 m thick, 1.5 m diameter, unsupported, plate. Material properties were identical to those used in the previous analysis. A 0.5 m thick plate was used in this analysis so that the P- and S-waves generated by the 25 μs contact time became separated as they propagated through the plate; this makes the displacement fields created by the waves easier to study.

The righthand side of figure 6 shows the displacement field in the plate 125 μs after the start of the impact. (Since the displacement field is axisymmetric, only half of the plate is shown.) At 125 μs the P-wavefront arrives at the epicenter of the plate. The position of the P- and S-wavefronts are indicated on the lefthand side of the figure. The magnitude and direction of the average nodal dis-

placement of each element is indicated by a vector. The relative lengths of the vectors depend on the magnitude of the largest displacement that occurs within the plate at a particular time. The vector lengths are also adjusted by a scale factor which is not under the user's control. Therefore, the vector plots shown in figures 6(a) and 7 are not drawn to the same scale; this must be remembered when comparing the figures.

As mentioned, motion in a P-wave is parallel to the direction of wave propagation. In figure 6, the vectors within the P-wave are oriented along rays emanating from the impact point. This orientation is consistent with the direction of motion. The magnitude of the displacements in the P-wave are not uniform along the spherical wave. Displacements are maximum near the centerline of the plate (the ray connecting the impact point to the epicenter) and they diminish to almost zero at the top surface of the plate. This pattern of displacements is in agreement with that shown in figure 2.
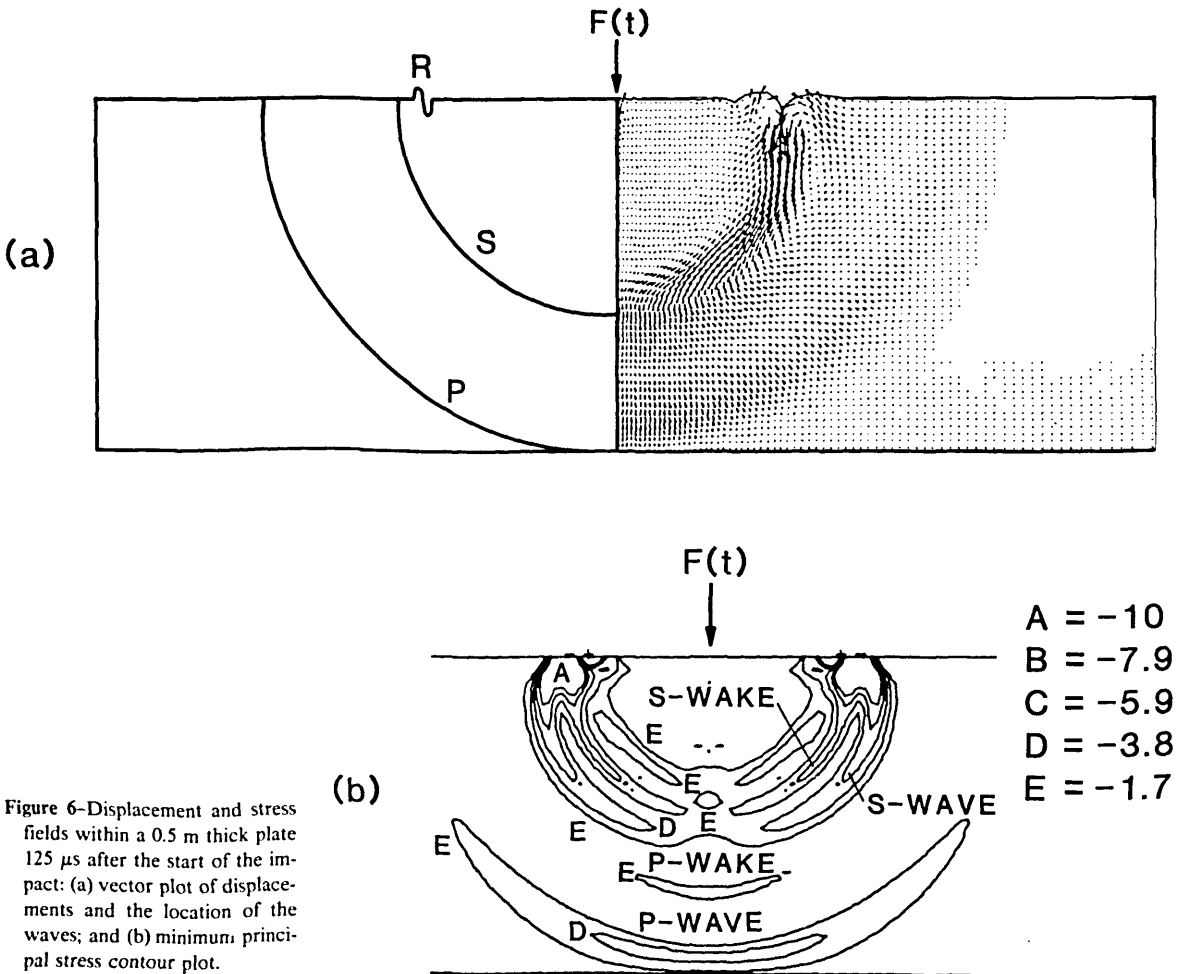
Figure 6–Displacement and stress fields within a 0.5 m thick plate 125 μs after the start of the impact: (a) vector plot of displacements and the location of the waves; and (b) minimum principal stress contour plot.

A = −10
B = −7.9
C = −5.9
D = −3.8
E = −1.7
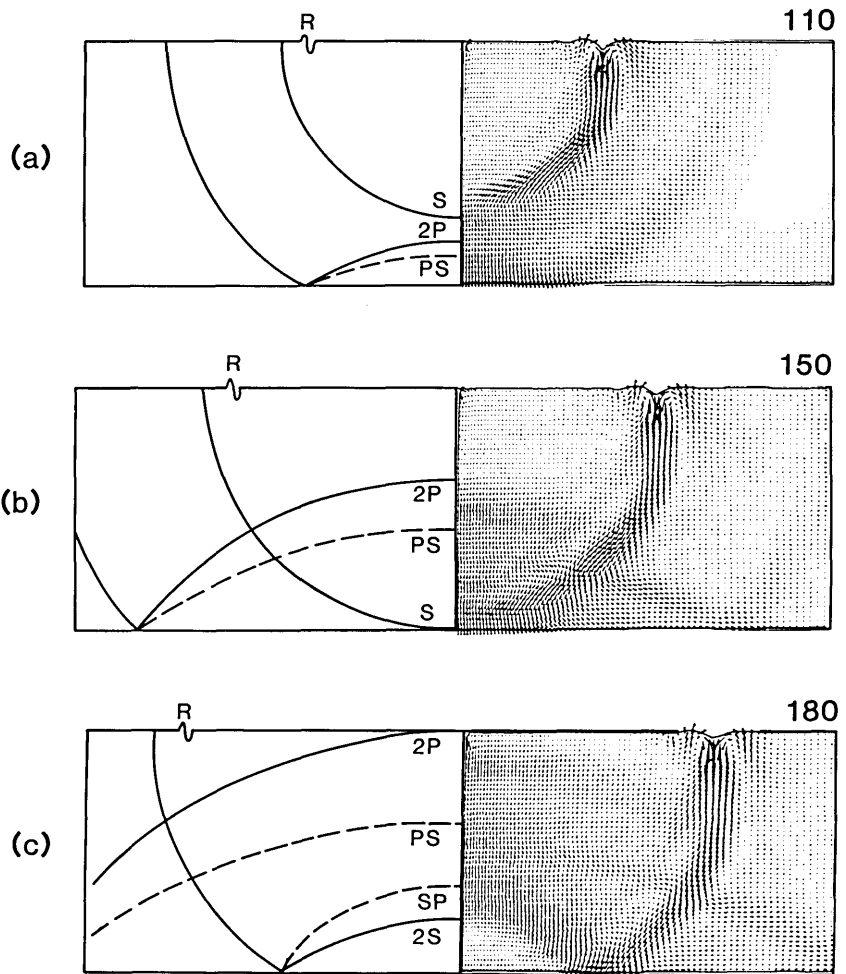
Figure 7–Vector plots of displacements at various times after the start of the impact: (a) 148 μs; (b) 203 μs; and (c) 250 μs.

The motion in an S-wave is perpendicular to the direction of wave propagation. In figure 6, the S-wave is easy to identify because of the orientation and large amplitude of the vectors within the wave. As expected, vectors are perpendicular to rays emanating from the impact point. Displacements along a spherical surface within the plate were studied to determine the effects caused by the S-wave. The displacements in the S-wave are approximately zero at the center of the plate and become larger along rays located at increasing angles from the centerline. A study of displacement time-histories obtained for various elements along a spherical front inside the plate showed that, near the critical angle (approximately 37 degrees from the centerline of the plate), there is a discontinuity in the displacements caused by the arrival of the S-wave; this discontinuity agrees with that predicted by the radiation pattern shown in figure 2. Near the surface, it is difficult to determine the amplitude of the displacements in the S-wave because

of interference due to the displacements caused by the R-wave. Note that in the vector displacement field all effects are superimposed; each vector represents the total displacement and direction of any given element.

Figure 6(b) shows a contour plot of minimum principal (compression) stress. The stresses in the P-wave are greatest at the centerline of the plate and decrease toward the surface. Since a state of pure shear stress is equivalent to a state of equal biaxial tension and compression, the plot of minimum principal stress also shows the stress variation in the S-wave. The stresses in the S-wave are lowest at the centerline and increase toward the surface. In the region near the surface of the plate, the stresses caused by the R-wave interfere with those produced by the S-wave making it difficult to separate the stresses caused by each wave.

The observed patterns of displacements and stresses in the P- and the S-waves are similar to those expected based on the displacement fields

produced by a harmonic point source (fig. 2). However, in addition to these P- and S-wave radiation patterns, figure 6(b) shows that in the region between the P- and S-waves there are stresses that resemble those that occur in a P-wave; this is the "P-wake." In addition, there is a region of nonzero displacements and stresses trailing the S-wave (the "S-wake") that resembles the patterns in the S-wave. Thus, the disturbances generated by impact on a plate are not confined in the P- and S-waves.

Figures 7(a) through 7(c) show displacement fields obtained from the finite element analysis, along with corresponding schematic representations of the position of the P-, S-, and the mode-converted PS- and SP-waves, at 148, 203, and 250 μs after the start of the impact.

The displacement field at 148 μs [fig. 7(a)], shows reflection of the P-wave at the bottom surface of the plate. The S-wave created by mode-conversion of the incident P-wave (referred to as the PS-wave) is not yet discernible as it is masked by the displacements caused by the reflected P-wave.

At 203 μs [fig. 7(b)], the S-wavefront arrives at the epicenter. The bottom surface of the plate is displaced downward at this time because of the effect of the preceding P-wave and P-wake. The S-wake is clearly visible.

At 250 μs [fig. 7(c)], the front of the reflected P-wave arrives at the top surface of the plate. The PS-wave is now easily discernible. Reflection of the S-wave is occurring and the mode-converted P-wave (referred to as SP) that was generated by the reflection of the incident S-wave is seen emerging from the front of the reflected S-wave. The SP-wave causes much larger displacements than the reflected S-wave.

Once multiple reflections of the P-, S-, and mode-converted waves begin to occur, the disturbances created by individual waves become more difficult to distinguish in the displacement fields.

Impact-Echo Response

The use of the impact-echo method for nondestructive testing involves interpretation of displacement waveforms obtained near the point of impact. In this section, a surface displacement waveform obtained from the Green's function solution for the impact response of an infinite plate is compared with results obtained by the finite element method.

Green's Function Solution: The normal displacement calculated at a point on the top surface of a infinite plate due to impact at another point on the same surface is shown in figure 8(a). This thickness,
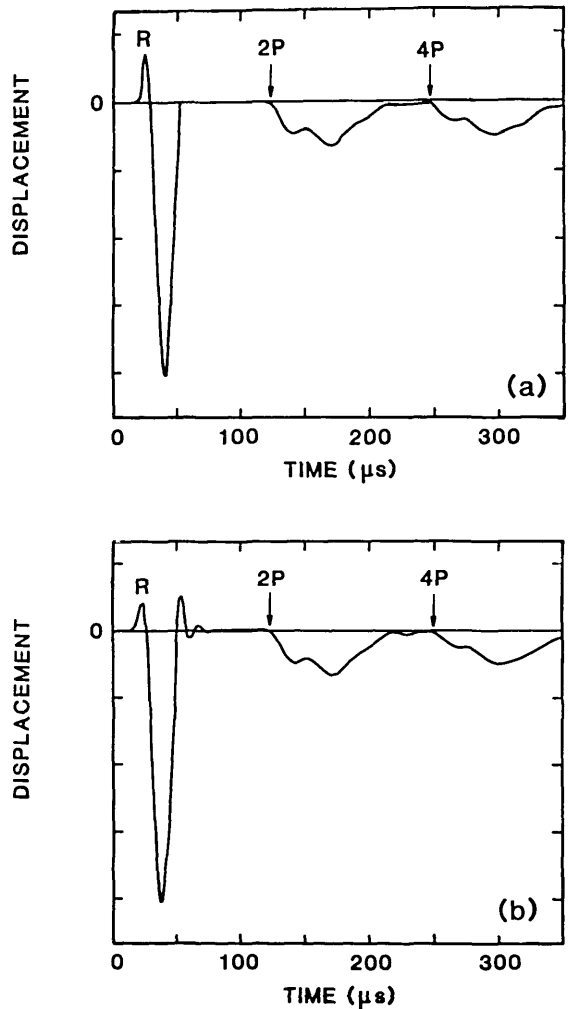
Figure 8–Impact-echo response: (a) Green's function solution; and (b) waveform obtained for finite element analysis.

T, of the plate was 0.25 m. The spacing, H, between the impact point and the point where the displacement was calculated (the point where a receiving transducer would be located) was 0.05 m [see fig. 3(b)]. The ratio of the S- to the P-wave speed was 0.61 and the contact time of the impact was 31 μs as in the epicenter analysis.

The waveform shown in figure 8(a) consists of displacements caused by the arrival of multiply reflected P- and S-waves and mode-converted waves. In addition, there is an initial large displacement caused by the R-wave propagating along the top surface of the plate. In the figure, the R-wave arrival is denoted by an R, and multiple P- and S-wave arrivals and mode-converted wave arrivals are indicated. For this particular configuration ($H/T=0.2$), the normal displacements caused by the S-wave are very small.

As discussed previously, the P-waves which arrive at the top surface are tension waves; the arrival of each tension wave pulls the surface downward. Thus the perturbations in the impact-echo response have a pattern similar to the epicenter response.

Comparison With Finite Element Solution: Figure 8(b) shows the displacement waveform obtained from the finite element analysis of the 0.25 m thick plate subjected to a 31 μs duration impact. The spacing between the impact and the point where the displacement waveform was recorded is 0.05 m as in the Green's function solution. Material properties are the same as those used in the previous analyses.

If the shape and relative magnitudes of the perturbations in the waveform obtained from the finite element analysis [fig. 8(a)] are compared with those in the Green's function solution [fig. 8(b)], it is seen that there is good agreement between the two waveforms.

As in the epicenter response obtained from the finite element analysis, low amplitude oscillations due to excitation of the zero energy modes of the finite elements occur in figure 8(b). After the R-wave has passed the receiver, the surface displacement should go to zero, as shown in figure 8(a), until reflections arrive from the bottom of the plate. However, the oscillations due to excitation of the zero energy modes cause the computed surface displacement to oscillate about zero for a short time. In this case, the zero energy modes are excited by the element distortion caused by the rapid, large changes in displacement that occur in the R-wave. This numerical ringing does not affect the echo pattern due to the multiply reflected waves.

Summary

The internal displacement and stress fields produced by a transient point load on the top surface of an elastic plate were studied using the finite element method. It was shown that in addition to P- and S-waves, intermediate displacement and stress fields (wakes) are produced by a transient point load applied normal to a stress-free boundary. Surface displacement waveforms computed by the finite element method showed good agreement with those obtained from the Green's function solution.

The study presented in this paper has demonstrated the potential of the finite element method for becoming a powerful tool for understanding the
interaction of stress waves with defects within solids. Such knowledge is essential for successful implementation of nondestructive testing techniques based on stress wave propagation, such as the impact-echo method under development at NBS. The power of the finite element method lies in its ability to analyze solids having arbitrary shapes, boundary conditions, and applied loads, and to generate complete pictures of displacement and stress fields in a computationally efficient manner. A subsequent paper will present finite element studies of the diffraction of transient stress waves by flat-bottom holes and circular disks within plates—problems for which no Green's function solutions currently exist.

References

[1] Carino, N. J., and M. Sansalone, Pulse-Echo Method for Flaw Detection in Concrete, National Bureau of Standards Technical Note 1199, 33 pp. (July, 1984).
[2] Carino, N. J., Laboratory study of flaw detection in concrete by the pulse-echo method, in *InSitu/Nondestructive Testing of Concrete*, ACI SP-82 edited by V. M. Malhotra, American Concrete Institute, 557–580 (1984).
[3] Carino, N. J.; M. Sansalone and N. N. Hsu, A point source–point receiver, pulse-echo technique for flaw detection in concrete, Journal of the American Concrete Institute, Vol. 83, No. 2, pp. 199–208 (April 1986).
[4] Carino, N. J., M. Sansalone and N. N. Hsu, Flaw detection in concrete by frequency spectrum analysis of impact-echo waveforms, *International Advances in Nondestructive Testing*, Vol. 12, pp. 117–146, W. McGonnagle, Ed., Gordon & Breach Science Publishers, New York, 1986.
[5] Kolsky, H., *Stress Waves in Solids*, Dover Publication, Inc.: New York (1963).
[6] Roderick, R. L., The radiation pattern from a rotationally symmetric stress source on a semi-infinite solid, Part II of Ph. D. Thesis, Grad. Div. of Appl. Math., Brown U., pp. 1–29 (May, 1951).
[7] Miller, G. F., and H. Pursey, The field and radiation impedance of mechanical radiators on the free surface of a semi-infinite solid, Proc. of the Royal Society of London, A, 223, pp. 521–541 (1954).
[8] Miller, G. F., and H. Pursey, On the partition of energy between elastic waves in a semi-infinite solid, Proc. of the Royal Society of London, A, 233, pp. 55–69 (1955).
[9] Pao, Y. H., and R. R. Gajewski, The generalized ray theory and transient responses of layered elastic solids, *Physical Acoustics*, Vol. XIII, Eds., W. P. Mason and R. N. Thurston, Academic Press: New York, 183–265 (1977).
[10] Johnson, L. J., Green's function for Lamb's problem,

Geophysical J. Royal Astro. Soc., Vol. 37, 99–131 (1974).

[11] Pao, Y. H.; R. R. Gajewski and A. N. Ceranogly, Acoustic emission and transient waves in an elastic plate, J. Acoust. Soc. Am., Vol. 65, 96-105 (1979).

[12] Gallagher, R. H., *Finite Element Analysis, Fundamentals*, Prentice-Hall, Inc.: Englewood Cliffs, New Jersey (1975).

[13] Hallquist, J. O., A Procedure for the Solution of Finite-Deformation Contact-Impact Problems by the Finite Element Method, UCRL-52066, Lawrence Livermore Laboratory, 46 pp. (April 1976).

[14] Goudreau, G. L., and J. O. Hallquist, Recent developments in large-scale finite element Lagrangian hydrocode technology, Computer Methods in App. Mechanics and Eng., Vol. 33, 725–757 (1982).

[15] Hallquist, J. O., User's Manual for DYNA2D—An Explicit Two Dimensional Hydrodynamic Finite Element Code With Interactive Rezoning, Lawrence Livermore Laboratory, Rev. (Jan. 1984).

[16] Hallquist, J. O., User's Manual for MAZE: An Input Generator for DYNA2D and NIKE2D (June 1983).

[17] Hallquist, J. O., User's Manual for ORION: An Interactive Post-Processor for the Analysis Codes NIKE2D, DYNA2D, and TACO2D (July 1983).

[18] Goldsmith, W., *Impact: The Theory and Practice of Colliding Solids*, Edward Arnold Press, Ltd., 24–50 (1965).

[19] Bracewell, R. N., *The Fourier Transform and Its Application*, 2nd Ed., McGraw-Hill Book Co.: NY (1978).

[20] Eitzen, D., et al., Fundamental Developments for Quantitative Acoustic Emission Measurements, EPRI NP–2089, RP 608-1, Interim Report, 262 pp. (Oct. 1982).

[21] Hsu, N. N., Dynamic Green's Function of an Infinite Plate—A Computer Program, NBSIR 85-3234, National Bureau of Standards, Gaithersburg, MD (Oct. 1985).

[22] Graff, K., *Wave Motion in Elastic Solids*, Ohio State University Press (1975).

[23] Flannagan, D. P., and T. Belytschko, A uniform strain hexahedron and quadrilateral with orthogonal hourglass control, Int. Journal of Numerical Methods in Engineering, Vol. 17, pp. 679–706 (1981).

A Finite Element Study
Of the Interaction of Transient
Stress Waves With Planar Flaws

Mary Sansalone, Nicholas J. Carino, Nelson N. Hsu

National Bureau of Standards
Gaithersburg, MD 20899

This paper presents a finite element study of transient wave propagation in plates containing planar flaws. The effects on displacement waveforms caused by waves diffracted from the sharp edges of a flaw are determined. Displacement fields within a plate containing a flat-bottom hole show the interaction of transient stress waves with a planar flaw. Waveforms obtained from the finite element analysis were compared with experimentally obtained waveforms.

Key words: concrete; finite element analysis; flaw; Green's function; impact; impact-echo method; nondestructive testing; wave propagation.

Introduction

A previous paper by the authors [1][1] presented a study of transient stress wave propagation in plates. In the previous work, the finite element method was used to study the displacement and stress patterns generated by a transient point load on a plate. Good agreement was found when surface displacement waveforms obtained from finite element analyses were compared with those obtained from the exact Green's function solutions for impact on an infinite plate. The discussion and results presented in reference [1] form the basis for finite element studies of transient stress wave propagation in solids containing defects—problems for which no exact solutions exist.

This paper presents finite element studies of the interaction of transient stress waves with planar discontinuities in an elastic solid. Emphasis is placed on the effects on displacement waveforms caused by waves diffracted from the edges of a flaw. An aluminum plate with a flat-bottom hole was chosen for the initial finite element studies because its geometry is simple and the physical specimen was easy to fabricate. This allowed the finite element results to be verified by comparison with experimentally obtained waveforms. Displacement waveforms obtained from analyses of planar, disk-shaped flaws in aluminum and concrete plates are presented.

Background

Figure 1 shows a schematic representation of point impact on a plate containing a planar disk-shaped flaw. The center of the flaw is located directly under the point of impact and the flaw is parallel to the top surface of the plate. Point impact is generated by dropping a small sphere onto the surface of the plate. The time-history of the contact

---

About the Authors: Mary Sansalone and Nicholas J. Carino serve with the Center for Building Technology, and Nelson N. Hsu is with the Center for Manufacturing Engineering. The two centers are part of the National Engineering Laboratory at NBS.

---

[1]Figures in brackets indicate literature references.
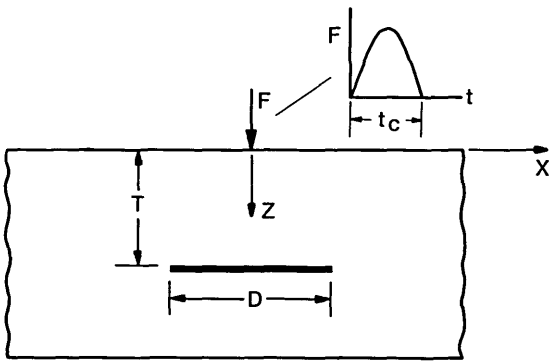
Figure 1–The important variables affecting the response of a planar disk-shaped void in a plate.

force generated by the elastic impact of a small sphere on a large plate can be approximated as a half-cycle sine curve (see fig. 1). This is the case that will be discussed in this paper. For this flaw geometry and impact time-history, the important variables affecting the response are the diameter, D, and depth, T, of the flaw, and the frequency content of the stress waves generated by impact. For a half-cycle sine curve time-history, the frequency content is determined by the contact time, t_c, of the impact [2]. A long contact time produces stress waves made up primarily of large amplitude, low frequency components. Stress waves produced by a short duration impact contain a broader range of frequencies in the waves; however, the amplitude of each component frequency is lower.

Figure 1 also shows the assumed coordinate axis. The positive z-direction will be referred to as the downward direction in this paper; the negative z-direction will be referred to as the upward direction.

When a transient stress wave is incident upon a crack within a solid, the following phenomena occur: specular reflection from the crack face; diffraction at the edges of the crack; and, mode conversion of waves on the crack face and at the edges of the crack. Figure 2(a) shows the specularly reflected P-wavefront (2P) and the mode-converted PS-wavefront produced when a spherical P-wave is incident upon a circular crack. Rays OA, which intersect the edges of the crack, will be diffracted as shown in figure 2(b), producing two diffracted waves, P_dP and P_dS. The designation used for diffracted waves includes the incident wave and the wave produced by diffraction. For example, P_dS is the designation for the diffracted S-wave that is produced by an incident P-wave. The diffracted waves propagate along wavefronts that

form a torus of circular cross section; the circumference of the crack is the center of the torus. A similar set of specular (2S), mode-converted (SP), and diffracted waves (S_dP and S_dS) are produced when the S-wave is incident upon a crack. The amplitude of particle motion in each of the specularly reflected, mode-converted, and diffracted waves varies with direction and depends upon the size, geometry, and depth of the crack, the frequency content of the waves incident upon the crack, and the orientation of the crack with respect to the propagating waves. As shown in figure 2(b), there is a region beneath the crack called the shadow zone, where direct P- and S-waves cannot penetrate.

Plate With a Flat-Bottom Hole

In the impact-echo method, a surface displacement waveform recorded near the point of impact is used to obtain information about wave reflection in the interior of the solid. When sharp internal discontinuities exist, the displacements caused by the arrival of diffracted waves are added to the displacements caused by the arrival of reflected waves. Correct interpretation of waveforms requires an understanding of the displacements caused by diffracted waves. In this study, the finite element method is used to gain this understanding. Analyses were performed using DYNA2D [4], a finite element program developed at Lawrence Livermore National Laboratory.

Experimental verification of the results obtained from the finite element analysis was necessary. Thus, a plate containing a flat-bottom hole was used for the initial studies since this test specimen could be easily fabricated.

In the discussion of the elastic response of a plate containing a flat-bottom hole to point impact on the top surface, the following analytical results are presented: 1) the displacement time-history of the surface of the hole directly under the point of impact; 2) displacement fields recorded at various times to show transient stress waves propagating within the plate; and 3) the displacement time-history of a point on the top surface of the plate, near the point of impact. To aid in understanding the effects of diffraction, the displacement time-histories obtained from the plate with a flat-bottom hole are compared to time-histories obtained from a solid plate. Finally, a displacement time-history obtained from a finite element analysis is compared to an experimentally obtained impact-echo displacement waveform.
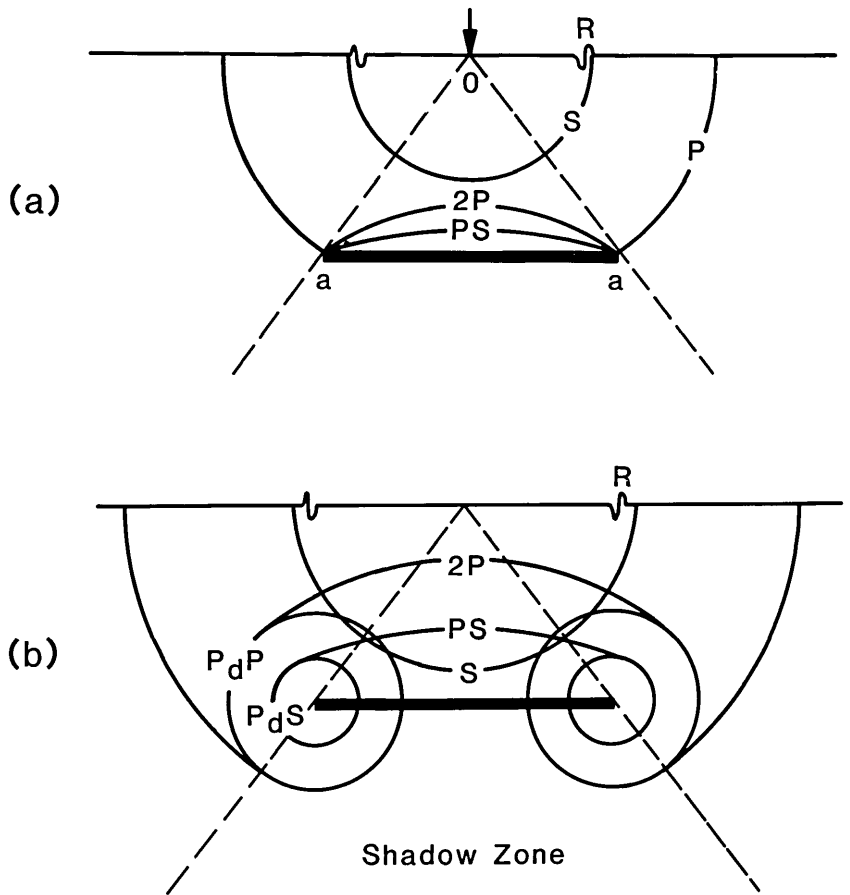
Figure 2–Diffraction at the edges of a crack: a) P-ray incident upon the edges of a crack; and, b) cylindrical wavefronts P_dP and P_dS emitted from tips.

The dimensions of the plate with the flat-bottom hole are shown in figure 3. The diameter, D, is 38 mm and the depth to the hole, T, is 38 mm; this geometry corresponds to a D/T value of 1. The axisymmetric, finite element model is shown on the right half of the figure. The plate is made of aluminum and the values of the material properties used in the analysis were: modulus of elasticity equal to 7.1×10^7 kPa, Poisson's ratio equal to 0.33, and density equal to 2700 kg/m^3. These values resulted in P-, S-, and Rayleigh (R) wave speeds of 6242, 3144, and 2930 m/s, respectively.

The axisymmetric finite element mesh was composed of three regions. These regions are shown on the left half of figure 3. The smallest elements are used above and near the edges of the hole. In Region 1, 0.75 mm square elements were used to construct the finite element model. In Regions 2 and 3, the 0.75 mm elements are made gradually larger as the distance from the hole increases.

The time history of the impact loading was a half-cycle sine curve with a 2 μs contact time ($t_c = 2$ μs). An important parameter used to characterize the impact is the ratio of the contact time of the impact, t_c, to the time it takes for the P-wave to propagate down through the plate, be reflected from the surface of the hole, and propagate back to the top surface of the plate, t_{2P} [2,3]. If the top of the hole is considered the reflecting interface, t_{2P} is equal to 12.2 μs; thus, t_c/t_{2P} is equal to 0.16. This small value was chosen so that displacements caused by various waves would be easier to distinguish. The transient load was applied as a uniform pressure over the two elements at the top of the plate adjacent to the centerline of the plate. In the analyses of aluminum plates discussed in this paper, values of displacement and stress were stored in data files every 0.2 μs.

Displacement Response at the Center of the Hole

The vertical displacement waveform obtained at the center of the flat-bottom hole (point A in fig. 3) is shown as a solid line in figure 4. This response
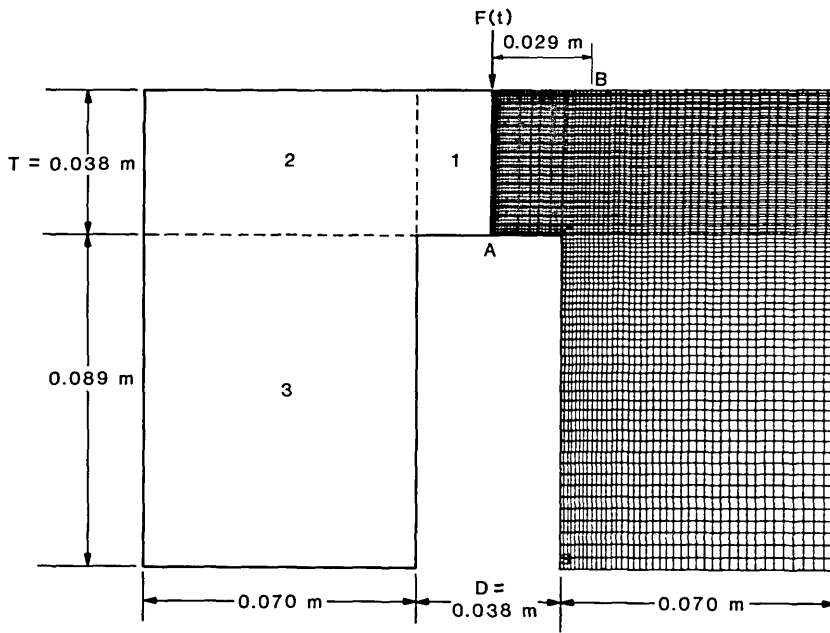
Figure 3-Finite element model of a plate with a flat-bottom hole.
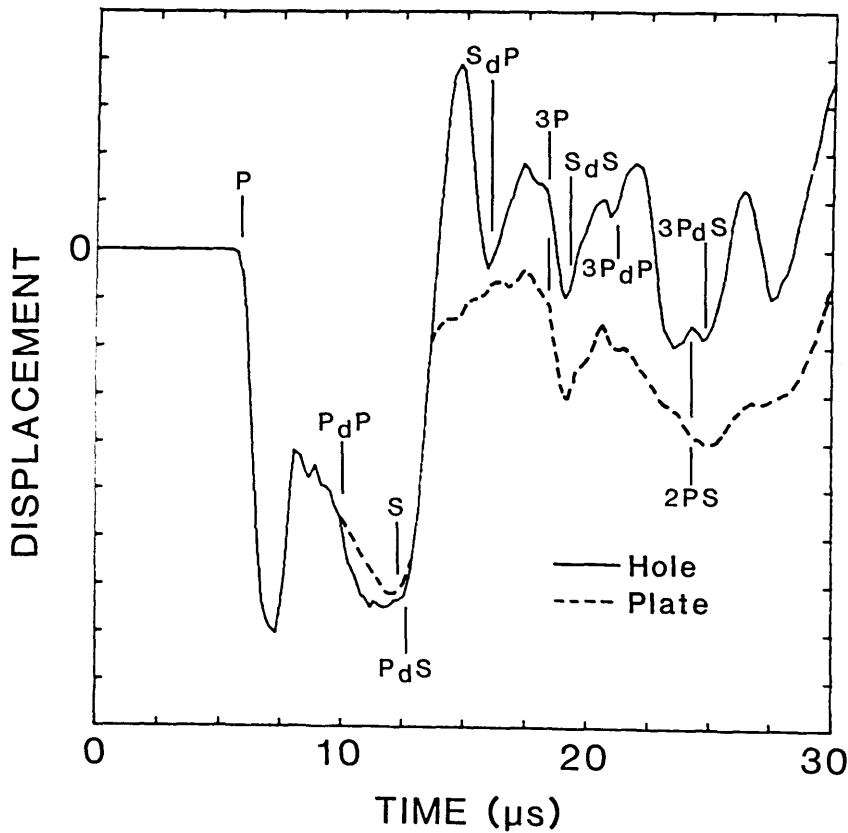
Figure 4-Displacement waveforms at the center of the flat-bottom hole and at the epicenter of a solid plate.

consists of vertical surface displacements caused by the arrival of the direct waves, multiply reflected waves (3P), mode-converted waves (2PS), and diffracted waves (P_dP, P_dS, S_dP, S_dS, $3P_dP$, etc.). The computed arrival times of the various waves are indicated on the waveform. The analysis was terminated before waves reflected from the sides and the bottom of the plate arrived at the hole.

For comparison, the dashed line in figure 4 shows the response of a point at the center of the bottom surface of a solid aluminum plate. The plate was 38 mm thick and was subjected to the same 2 μs duration impact used in the analysis of the plate containing the flat-bottom hole. The finite element mesh for the plate was comprised of Regions 1 and 2 of the mesh shown in figure 3; that is, the elements below the top surface of the hole were eliminated. The vertical surface displacement for the plate consists of displacements caused by direct, multiply reflected, and mode-converted waves. (In ref. [1] the plate response was discussed in detail.) The waveform obtained from the flat-bottom hole (solid line in fig. 4) is the superposition of this plate response and the displacements caused by diffracted waves. Thus, the differences between the waveforms shown in figure 4 are due to the displacements caused by diffracted waves from the edges of the flat-bottom hole.

Using the waveform obtained from the plate (dashed line) as a baseline response, that is, the component of the response common to both waveforms, the effect of the diffracted waves on the displacement pattern can be determined. The arrival of diffracted wave P_dP produces a noticeable change in the displacement pattern, but causes only a slight increase in the magnitude of the displacement compared with the baseline response. The P_dS-wave causes an upward displacement of the surface which pushes the surface of the hole well above its original undisturbed position. The S_dP-wave also produces an upward displacement of the hole; however, the magnitude of this displacement is less than that produced by P_dS. The S_dS-wave causes an increase in the magnitude of the upward displacement that occurs after the 3P-wave. Arrivals of subsequent diffracted waves ($3P_dP$ and $3P_dS$) produce noticeable displacements in the waveform obtained from the hole (solid line) that are absent in the waveform obtained from the plate (dashed line). Thus, for this particular flat-bottom hole geometry and for the 2 μs duration impact used in the analysis, relatively large amplitude diffracted waves are produced which significantly alter the displacement pattern obtained at the center

of the hole compared with that obtained at the bottom of a solid plate.

Displacement Fields

The right sides of (a) and (b) of figure 5 show vector plots of the displacement fields in the plate containing the flat-bottom hole at 6.1 and 10 μs, respectively, after the start of the impact. (Since the displacement field is axisymmetric, the field for only half of the specimen is shown.) The corresponding positions of the P-, S-, mode-converted, and diffracted wavefronts are indicated on the left hand side of each figure.

The displacement field at 6.1 μs [fig. 5(a)] shows the P-wavefront arriving at the hole. The S-wavefront has traveled approximately half the distance to the hole. The pattern of displacements between the P- and the S-waves, and the P-wake, which was discussed in ref. [1], is evident.

Figure 5(b) shows the displacement field at 10 μs. The reflected P-wave (2P) is evident. The mode-converted PS-wave, produced by the incident P-wave, is difficult to distinguish as it overlaps the S-wave. The surface of the hole is displaced downward due to the displacements caused by the preceeding P-wave and the P-wake, which at 10 μs is incident upon the hole (see fig. 4). The pattern of displacements trailing the S-wave, the S-wake is evident (see ref. [1]). The low amplitude head wave can also be distinguished. Diffracted waves P_dP and P_dS have been produced by the P-wave incident at the edge of the hole. The P_dP-wave is clearly evident in the shadow zone behind the hole (fig. 5(b)) where the direct P-wave cannot penetrate. The pattern of displacements caused by the P_dS-wave is easy to distinguish.

To show the effects of the diffracted waves on the displacement response at the hole, close-ups of the region near the hole are shown on the right side of figures 6(a) through 6(c). These vector plots represent the displacement fields at 12, 13.5, and 15 μs after the start of the impact. The positions of the wavefronts in this region are shown on the left side of each figure.

In the displacement field at 12 μs (fig. 6(a)), the S-wave is incident on the center of the hole. The P_dP-waves are overlapping in the region above the hole.

Figure 6(b), the displacement field at 13.5 μs, shows the S-wave incident upon the edge of the hole. In the radiation pattern of the S-wave [1], vertical displacements in the center of the plate are very small; therefore, the S-wave does not cause significant downward movement of the center re-
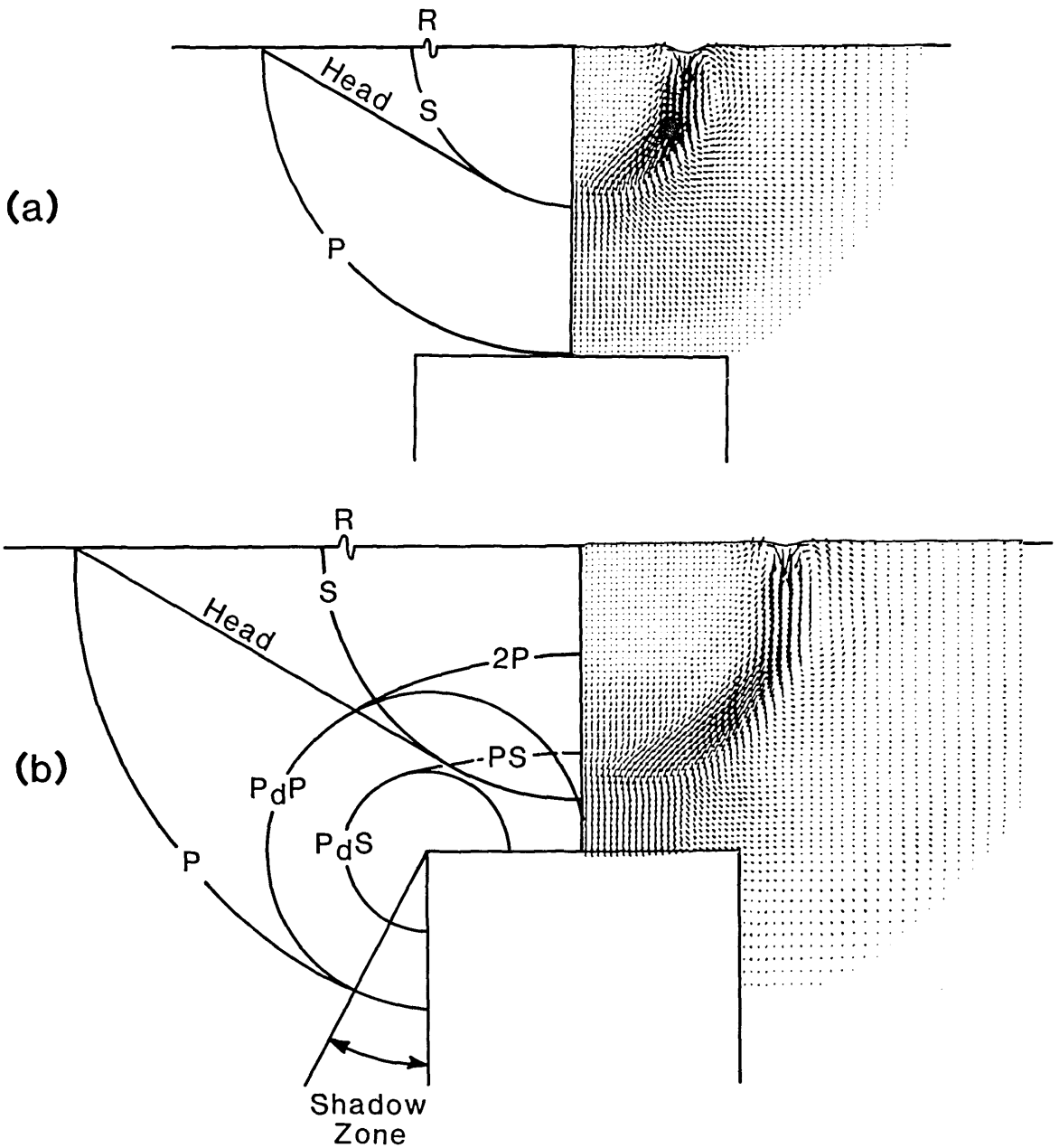
Figure 5–Vector plots of the displacement fields in a plate with a flat-bottom hole: a) 6.1 μs after the start of impact; and b) 10 μs after the start of impact.

gion of the hole. Thus, at 13.5 μs the center region of the hole is recovering and moving upward. At larger angles in the radiation pattern, the vertical component of the displacement in the S-wave increases. Thus, the outer region of the hole is depressed by the incident S-wave. The fronts of diffracted waves P_dS (one from each edge) have just arrived at the center of the hole. Recall that in the displacement waveform shown by the solid line

in figure 4, it was P_dS that produced the large upward displacement that pushed the center of the hole well above its original undisturbed position. In figure 4, at 13.5 μs the center of the hole is moving rapidly upward, but it is still displaced below its undisturbed position.

At approximately 15 μs the upward displacement of the center of the hole has reached its maximum (see fig. 4). The center of the hole is
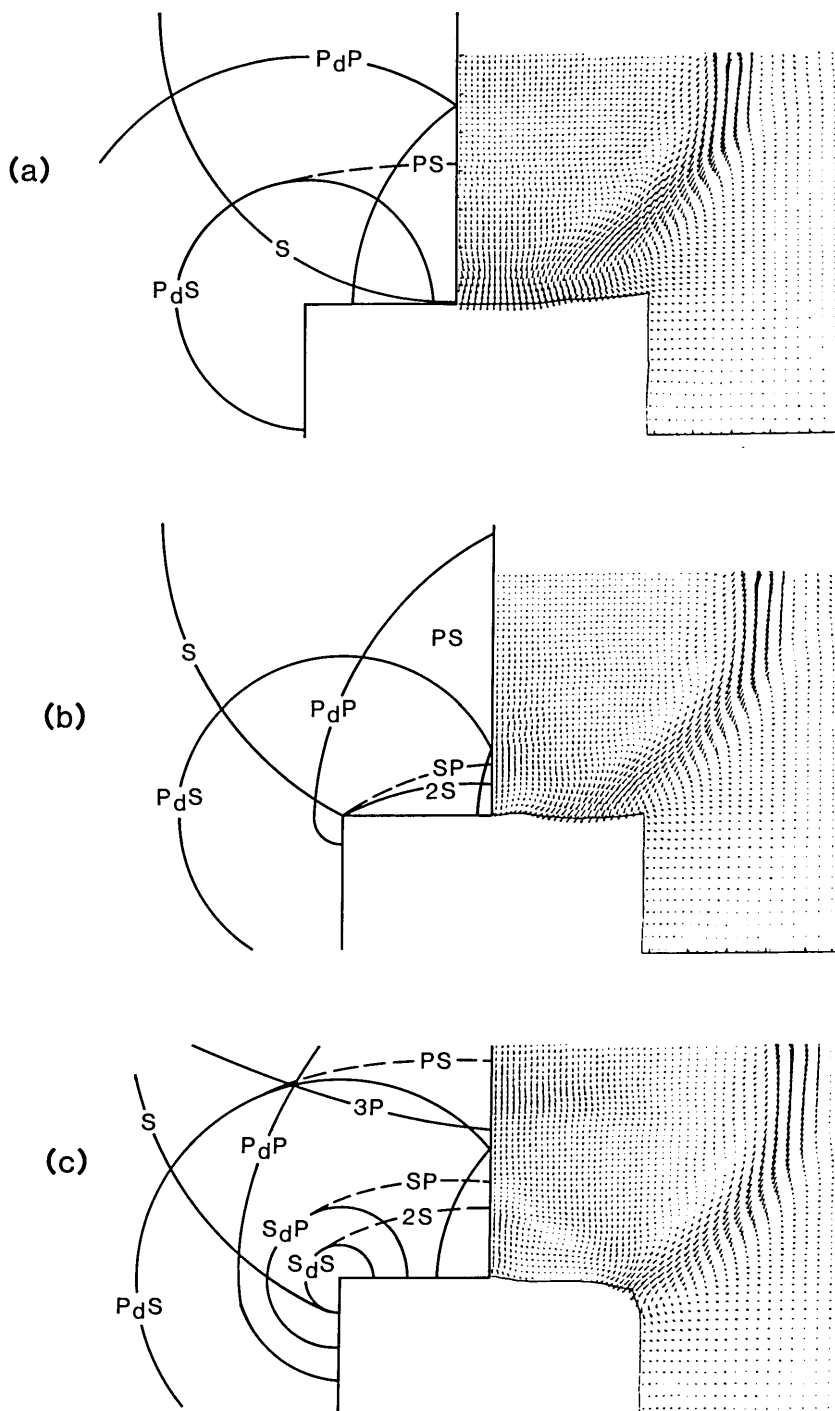
Figure 6–Close-ups of vector plots of displacement fields around the flat-bottom hole at various times after the start of impact: a) 12 μs; b) 13.5 μs; and c) 15 μs.

displaced upward, while the edge of the hole is pushed down by the incident S-wave. The diffraction pattern has become complicated; at 15 μs four diffracted wavefronts have been produced by the incident P- and S-waves. Each of these diffracted waves will give rise to new diffracted waves when they reach the opposite edge of the hole. These doubly diffracted wavefronts appear to be of secondary importance. The arrival of multiple reflected P- and S-waves from the top surface of the solid, such as the 3P-wave [seen at the top of fig. 6(c)], will also produce diffracted waves. In addi-

tion, diffracted waves will be reflected from the top surface of the plate giving rise to new diffracted waves when they strike the edge of the hole.

Impact-Echo Response

Displacement responses recorded on the top surface of a plate are referred to as impact-echo waveforms. Impact-echo waveforms obtained from both the plate with the flat-bottom hole and the solid plate can be used to determine the effects caused by diffracted waves on the displacement response at the top surface. The effects caused by diffracted waves can be more difficult to determine at the top surface of the plate than at the center of the hole, because surface waves often mask the effects caused by the specularly reflected and diffracted waves. However, since the relative wave arrival times of surface waves, reflected waves, and diffracted waves differ at increasing distances from the impact point, the problem can be overcome by studying waveforms obtained at different points along the surface.

A finite element study of impact-echo waveforms obtained from the plate with the flat-bottom hole showed that P_dP, P_dS, S_dP, and S_dS all cause upward movement of the top surface of the specimen. This is in contrast to the downward displacements caused by specularly reflected P-waves. Displacement waveforms represent the superposition of displacements caused by specularly reflected and diffracted waves. Thus, depending upon the arrival times of the diffracted waves relative to the specularly reflected waves, the effect of a diffracted wave can be to lessen or increase the displacements caused by specularly reflected waves. As an example, the solid line in figure 7 shows a displacement waveform obtained on the top surface of the plate containing the flat-bottom hole. The separation, H, between the impact point and the point where the response was recorded was 25 mm (point B in fig. 3). The response consists of displacements caused by the arrivals of direct P-, S-, and R-waves propagating along the surface, reflected P- and S-waves (2P, 2S, 4P), mode-converted waves (PS), and diffracted waves (P_dP, P_dS, S_dP, S_dS, etc.). The arrival times of these various waves are indicated on the waveform. In the figure, arrival times of diffracted waves correspond to the arrival of waves diffracted from the point on the edge of the hole nearest the receiver; these diffracted waves produce the most significant effects in the displacement response.
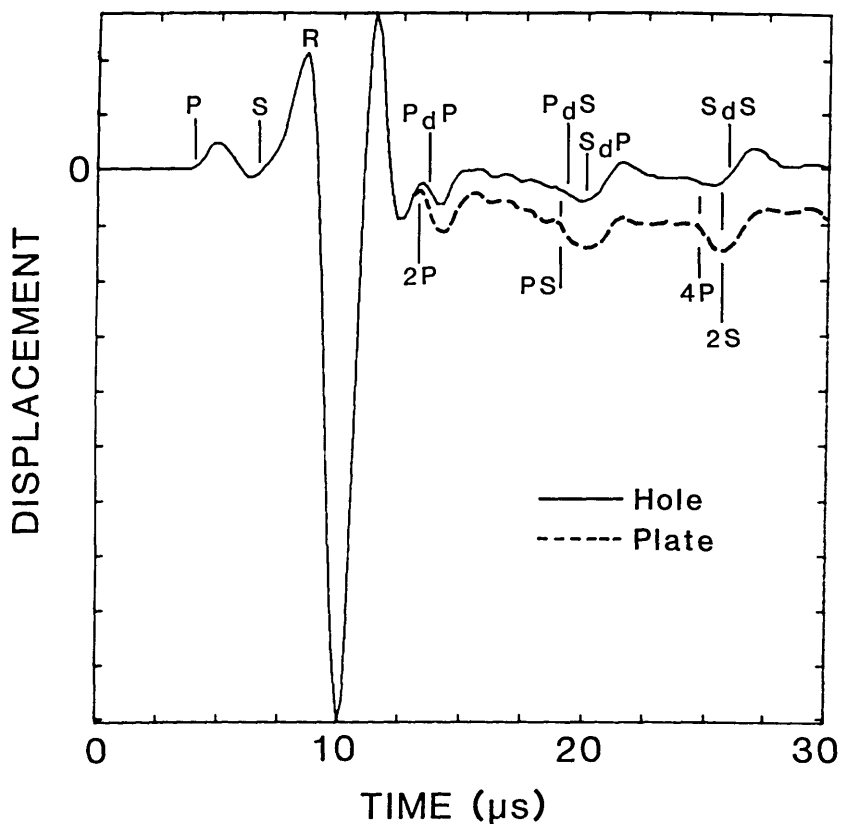
Figure 7–Impact-echo displacement waveforms from a plate with a flat-bottom hole and from a solid plate.

For comparison, the dashed line in figure 7 shows an impact-echo response that was obtained from the analysis of the 38 mm thick plate subjected to a 2 μs duration impact. As for the plate containing the flat-bottom hole, the separation between the impact point and point where the waveform was recorded was 25 mm. In the portion of the waveform after the R-wave signal, the response is dominated by the arrival of P-waves, which cause downward displacements; the top surface is never displaced above its undisturbed position.

From a comparison of the waveforms in figure 7, it is concluded that the diffracted waves cause the following effects: P_dP noticeably reduces the downward displacement caused by the 2P-wave; P_dS appears to have little effect, although it slightly reduces the downward displacement caused by the PS-wave; S_dP and S_dS both cause upward displacements.

If another point on the top surface of the plates had been chosen for this comparison, the displacement response caused by superposition of the specular and diffracted waves would be different, since both the arrival times and the amplitudes of the waves change relative to one another.

Comparison to Experimentally Measured Waveform

No exact solutions are available to compare with the finite element displacement waveforms; therefore, the finite element solution was compared to an experimentally obtained waveform. An impact-echo test was carried out on an aluminum plate containing a flat-bottom hole with dimensions as shown in figure 3. The impact point was located at the center of the specimen, and the spacing between the impact and receiving transducer was 29 mm. The impact source was a 1.6 mm diameter steel ball that was dropped from a height of 30 mm. The contact time of the impact was 10 μs. A broadband displacement transducer, developed at NBS for acoustic emission testing [5], was used as the receiver. This transducer is composed of a small conical PZT sensing element attached to a large brass cylinder, and has a uniform frequency response up to 1 MHz. The output of this transducer is proportional to normal surface displacement. The small 1.5 mm diameter of the conical tip of the transducer approximates a point receiver. Figure 8(a) shows the experimental waveform up to a time of 60 μs. The waveform includes reflections from the sides and bottom of the plate. At 40 μs the P-wave reflection from the bottom of the plate arrives at the receiver causing a large downward displacement; at 52 μs the R-wave reflected from the

side of the plate arrives at the receiver also causing a large downward displacement.

Figure 8(b) shows a displacement waveform obtained from a finite element analysis of the plate containing the flat-bottom hole subjected to an impact having a force-time history in the shape of a half-cycle sine curve with a contact time of 10 μs. The spacing between impact point and the point where the displacement was recorded was also 29 mm.

There is good agreement between the experimental response and the response predicted by the finite element analysis. The 10 μs duration impact results in a t_c/t_{2P} value of approximately 0.8. For this contact time and for the spacing between the impact point and the receiver, effects due to individual wave arrivals are difficult to discern [3]. The superposition of effects causes the arrival of the initial internal reflections to be hidden in the response of the surface to the large amplitude R-wave. However, the important feature in both waveforms
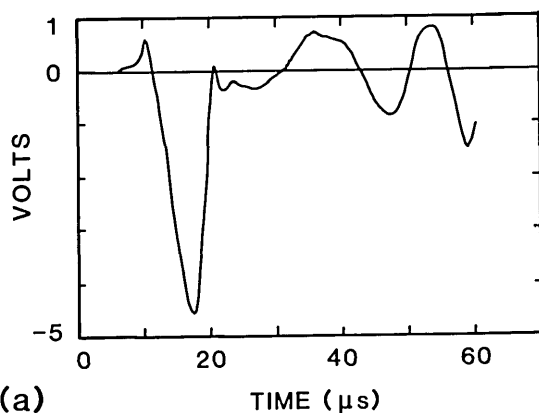
(a)
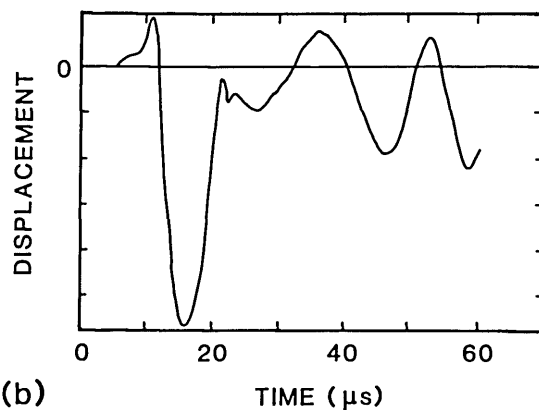
(b)

Figure 8-Comparison of analytical response with experimentally obtained response for a plate with a flat-bottom hole: a) experimental waveform; and, b) finite element waveform.

is that effects caused by diffracted waves move the surface above its undisturbed position.

This comparison established the validity of using the finite element method for modeling transient wave propagation in elastic solids containing flaws. Thus, the finite element method can be used to study the interaction of transient waves with flaw geometries more likely to be encountered in actual materials. In the following section, the discussion of a plate containing a flat-bottom hole is extended to study a similar, but more realistic, geometry—a plate containing a planar, disk-shaped flaw.

Planar Disk-Shaped Flaws in Plates
Flaw in Aluminum

The dimensions of an aluminum plate containing a disk-shaped flaw are identical to those shown in figure 3 for the plate containing the flat-bottom hole. The depth to the top surface of the flaw and the diameter of the circular flaw are identical to the depth to the top surface of the hole and the diameter of the flat-bottom hole. The finite element model was created by using the mesh shown in figure 3 with the addition of the elements required to form an interior disk-shaped void from the hole. The void was 1 mm thick. The analysis was carried out using the same material properties and loading conditions as in the analysis of the plate with the flat-bottom hole.

Displacement waveforms obtained at the center of the top surface of the flaw (point A in fig. 3) and at a point on the top surface of the plate, 25 mm from the point of impact (point B in fig. 3), are shown in figures 9(a) and (b), respectively. Wave arrival times are indicated on both waveforms. These waveforms do not need detailed explanation as they are very similar to those obtained from the plate containing the flat-bottom hole [figs. 4(a) and 7(a)]. A comparison of the waveforms obtained at the surfaces of the hole and the disk-shaped flaw shows that there are minor differences in the responses which occur after the arrival of the S_dS- and 2PS-waves. At the top surface the waveforms are almost identical, except that the displacements obtained from the plate containing the disk-shaped flaw are shifted slightly above those obtained from the plate with the flat-bottom hole. Thus, it appears that the presence of the material below the flaw does not significantly change the overall response for the period of time prior to wave reflections from the bottom of the plate.

The displacement patterns that have been discussed were obtained for planar flaws in aluminum.

Aluminum has a Poisson's ratio of 0.33 which results in a ratio of S- to P-wave speeds of 0.50. As mentioned, aluminum was used so that waveforms obtained from the finite element analysis could be compared to waveforms obtained from an easily fabricated test specimen. However, the primary focus of the research program is in applying the impact-echo method to concrete, a material with a Poisson's ratio of approximately 0.2 in the elastic range. For a Poisson's ratio of 0.2, the S-wave speed is 61% of the P-wave speed; this ratio is sig-
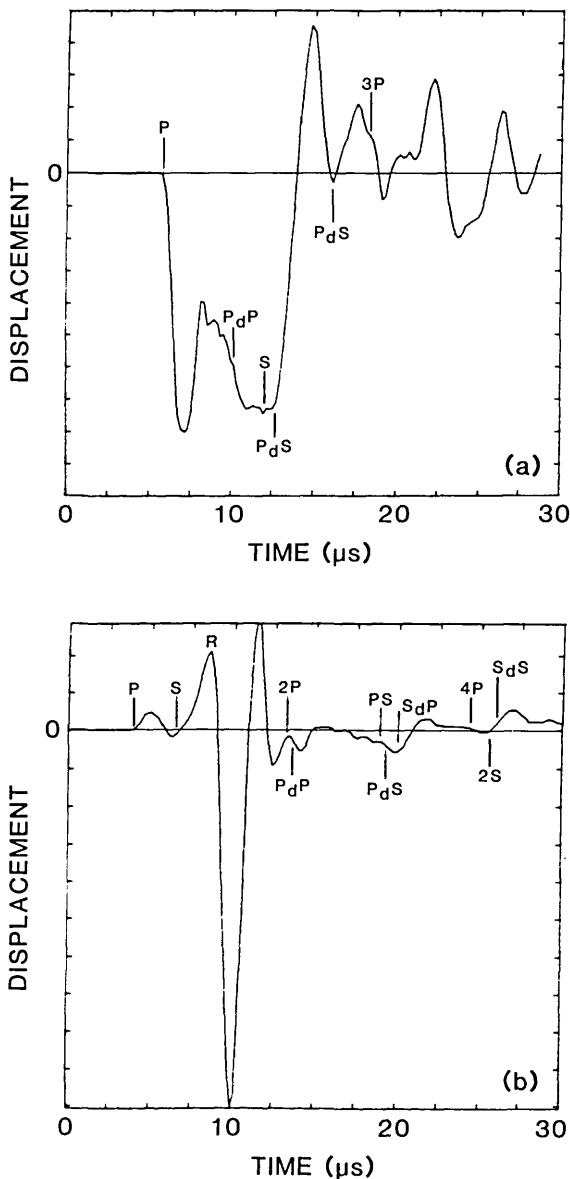
Figure 9–Planar disk-shaped flaw in an aluminum plate: a) displacement at the center of the top surface of the flaw; and, b) displacement at a point on the top surface of the plate.

nificantly different from that in aluminum. This difference affects the relative arrival times of the various wavefronts. For comparison, the displacement patterns obtained from a finite element analysis of a planar disk-shaped flaw in a plate having elastic properties representative of concrete are presented.

Flaw in Concrete

An analysis was performed for a planar, disk-shaped void in a 0.5 m thick concrete plate. The diameter and the depth of the flaw are both 0.2 m resulting in a D/T value equal to 1, the same D/T value as in the analyses of the flaws in aluminum. The concrete was modeled as a linearly-elastic, homogeneous solid, with the following material properties: modulus of elasticity of 3.31×10^7 kPa, Poisson's ratio of 0.2, and a density of 2300 kg/m³. These values result in P-, S-, and R-wave speeds of 4000, 2440, and 2240 m/s, respectively. In the Region 1, 5 mm square elements were used in the finite element model. The time history of the impact load was a half-cycle sine curve with a 16 µs contact time, which gave the desired ratio of t_c/t_{2P} equal to 0.16.

Displacement waveforms obtained at the center of the top surface of the flaw and at a point on the top surface of the plate, 50 mm from the impact point, are shown in figures 10(a) and (b), respectively. Wave arrival times are indicated on the waveforms. The displacement caused by each wave is the same as has been discussed; however, since there is less of a difference between the P- and S-wave speeds, individual wave arrivals in concrete are more closely spaced than in aluminum. Thus, the displacement waveforms obtained from the concrete specimen are different from those previously shown for the same flaw in aluminum. For example, compare the displacement pattern in figure 9(a) with that in figure 10(a). In the concrete specimen, the P_dS-wave arrives somewhat later than the PS-wave, rather than at approximately the same time as in the aluminum plate; thus, the large upward displacement caused by the P_dS-wave is easily identified in figure 10(a). As in aluminum, if the response obtained from the concrete plate containing the disk-shaped flaw is compared to the response obtained from a solid concrete plate [such as in fig. 5 of ref. [1]], the effects caused by diffracted waves are clearly evident. Diffracted waves produce more frequent fluctuations in the displacement and they move the top surface of the flaw above its undisturbed position. For the top surface displacement shown in

figure 10(b), the most noticeable effect due to diffracted waves is the large upward surface displacement caused by the arrivals of the P_dS- and S_dP-waves.

In figure 10(b), there is a period after the arrival of the R-wave when the displacement appears to oscillate about its undisturbed position. These oscillations are due to numerical ringing of the finite elements which occurs due to rapid changes in displacement [1].
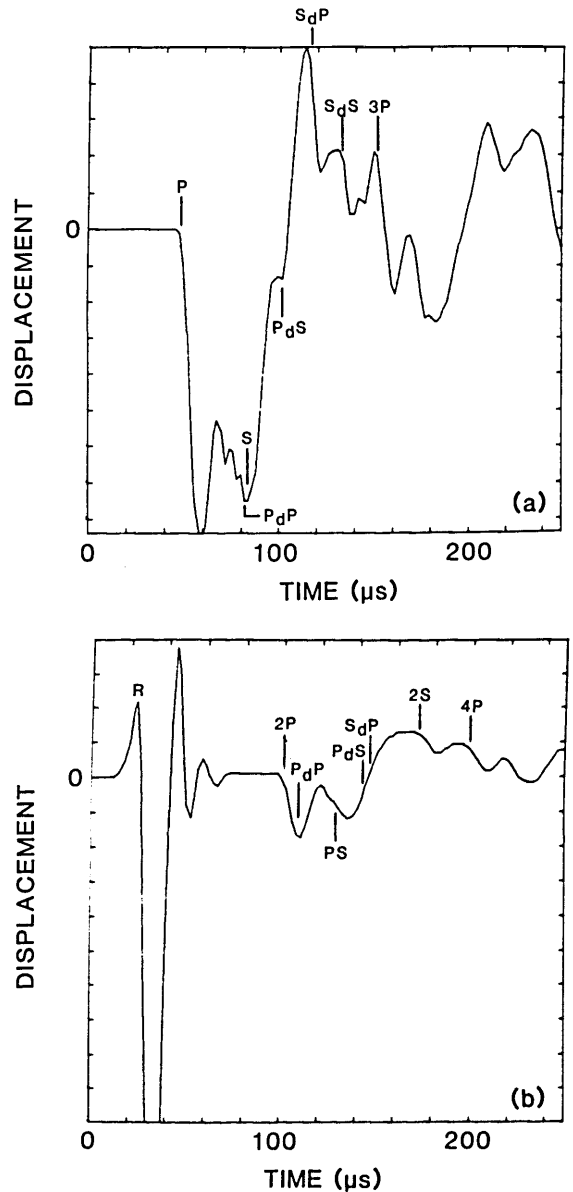
Figure 10–Planar disk-shaped flaw in a concrete plate: a) displacement at center of the top surface of the flaw; and, b) displacement at a point on the top surface of the plate.

Summary

A previous finite element study of the displacement and stress fields created by a transient point load on an elastic solid [1] served as the basis for the present study of the displacement fields created by the interaction of transient stress waves and planar flaws in solids. The elastic responses produced by surface impact on aluminum and concrete plates containing flat-bottom holes and planar disk-shaped flaws were studied. Displacement waveforms obtained from the plates were compared to waveforms obtained from solid plates to determine how displacement patterns are affected by the waves created by diffraction at the sharp edges of a discontinuity. It was shown that the displacement waveforms obtained from a plate with a flat-bottom hole are very similar to those obtained from a plate containing a planar disk-shaped flaw.

In this and the previous paper, comparisons of finite element waveforms to exact and experimentally obtained displacement waveforms established the validity of using finite element analysis for the study of transient wave propagation in elastic solids. These papers have laid the groundwork for using the finite element method to study elastic solids of arbitrary geometry and to study solids containing a variety of types of flaws—problems for which no exact solutions exist.

References

[1] Sansalone, Mary; Nicholas J. Carino and Nelson N. Hsu, A finite element study of transient wave propagation in plates, NBS Journal of Research, Vol. 92, No. 4 (1987).

[2] Carino, Nicholas J.; Mary Sansalone and Nelson N. Hsu, Flaw detection in concrete by frequency spectrum analysis of impact-echo waveforms, *International Advances in Nondestructive Testing*, Vol. 12, pp. 117–146, W. J. McGonnagle, Ed., Gordon & Breach Science Publishers: New York (1986).

[3] Carino, Nicholas J.; Mary Sansalone and Nelson N. Hsu, A point source—point receiver technique for flaw detection in concrete, Journal of the American Concrete Institute, Vol. 83, No. 2, pp. 199–208.

[4] Hallquist, John O., User's Manual for DYNA2D—An Explicit Two Dimensional Code with Interactive Rezoning, Lawrence Livermore Laboratory, Rev. (January 1984).

[5] Proctor, Thomas M., Jr., Some Details of the NBS Conical Transducer, Journal of Acoustic Emission, Vol. 1, No. 3, pp. 173–178 (1982).

Conferences / Events

REPORT ON THE INTERIM MEETING OF THE NATIONAL CONFERENCE ON WEIGHTS AND MEASURES JANUARY 12-16, 1987

The National Conference on Weights and Measures (NCWM) is a standards-writing organization that dates its establishment back to January 16, 1905, when the Director of the National Bureau of Standards hosted the first meeting of nine State representatives "in order to bring about uniformity in the state laws referring to weights and measures, and also to effect a close cooperation between the state inspection services and the National Bureau of Standards...." Today, all the NCWM technical committees and task forces meet at NBS in January of each year at what is called the "NCWM Interim Meeting" to study issues and make recommendations on weights and measures concerns, particularly the regulation of the commercial marketplace—scales, liquid meters, and prepackaged commodities. The active membership of the NCWM meet annually in July to vote on the Committees' recommendations. The Interim Meeting of the 72d NCWM (gaps in Annual Meetings occurred during both world wars) was held January 12-16, 1987. A summary of the most significant work of each major committee follows.

The Executive Committee manages the NCWM, sets policy, and sits as the Board of Governors of the National Type Evaluation Program (NTEP). The NTEP is a program of cooperation between NBS, NCWM, States, and the private sector for determining conformance of measuring devices with codes and other legal design criteria. A survey indicates that the program is accepted in all but three States in the United States. This year, the Executive Committee is revising the Policy and Procedures under which NTEP operates. Of special significance was the completion of plans for the evaluation of load cells used in commercial weighing devices. The NBS Automated Production Technology Division will provide the technical oversight for this activity. In addition, the Executive Committee is recommending new policies for interaction with the International Organization for Legal Metrology (OIML) in order to communicate the work of the OIML to a broader audience within the U.S.

The Committee on Laws and Regulations develops and interprets standards that are recommended for adoption by States as laws and regulations. This year, the Committee is proposing adoption by the NCWM of a Uniform Motor Fuel Law. This law incorporates ASTM standards on gasoline, diesel fuel, and gasoline-alcohol blends. In addition, the Committee is recommending test methods for packaged commodities subject to moisture loss.

The Committee on Specifications and Tolerances develops standards that are adopted by States as device code requirements and test methods. At the 1987 Interim Meeting, the Committee determined how the NCWM will set standards and test procedures to deal with the problem of gasoline vaporization during tests of "loading-rack" (wholesale gasoline delivery) meters.

The Committee on Education promotes the education and training of weights and measures officials for an increasingly technologically-sophisticated marketplace. It has managed the development of a series of training "modules" under a grant from the NBS. The Committee has proposed minimum qualifications this year for selecting

instructors to deliver the training using the modules.

The Committee on Liaison represents the NCWM to the Federal Government and other organizations. At the 1987 Interim Meeting, the Committee agreed to petition the Department of Treasury, Bureau of Alcohol, Tobacco, and Firearms to modify their regulations for malt beverages to conform to Federal and State labeling requirements covering other types of packaged goods.

The 72d Annual Meeting of the NCWM will be held in Little Rock, Arkansas July 19–24, 1987. Approximately 400 representatives from government and industry are expected to attend. The NBS will publish the proceedings of the meeting as a special publication, and publish updates of the weights and measures handbooks, Handbook 44 "Specifications, Tolerances, and Other Technical Requirements for Weighing and Measuring Devices," Handbook 130 "Uniform Laws and Regulations," and Handbook 133 "Checking the Net Contents of Packaged Goods" as a result of voting at the Annual Meeting.

For further information call or write Albert D. Tholen, Office of Weights and Measures, Office of Product Standards Policy, National Bureau of Standards, Gaithersburg, MD 20899.

Carroll S. Brickenkamp
Office of Weights and Measures
Office of Product Standards Policy
National Bureau of Standards
Gaithersburg, MD 20899

Conferences / Events

FIFTEENTH PLENARY MEETING OF ISO/TC 108 ON MECHANICAL VIBRATION AND SHOCK

The fifteenth plenary meeting of the International Standards Organization (ISO)/Technical Committee (TC) 108 on Mechanical Vibration and Shock was held at NBS Gaithersburg from March 30 through April 10, 1987. Approximately 130 delegates from 15 countries participated in the two weeks of meetings of the technical committee, its four subcommittees, and nearly all of its 27 working groups.

The American National Standards Institute (ANSI), the U.S. member body, has held the secretariat for this committee since the latter was established in 1963. Presently, 17 countries are participating and 26 others are observer members. The committee maintains liaison with other TC's of ISO and of the International Electrotechnical Commission (IEC). The chairman for the current term is Robert G. Bartheld of Siemens Energy & Automation; the secretary is Avril Brenig, standards manager of the Acoustical Society of America, which organization has administered the TC 108 Secretariat on behalf of ANSI.

Opening the plenary session, the director of NBS, Ernest Ambler, reviewed the contributions to standardization of ISO in general and of TC 108 in particular; he also stressed the communality of interests between NBS and the voluntary standards community. The working meetings that followed addressed standardization in such diverse areas as balancing machines, vibration control on vehicles and structures, calibration of vibration and shock measuring instruments, and evaluation of human exposure to mechanical shock and vibration. Those standards ranged from some very specific problems, such as "rotor-shaft-key convention," to rather general ones, like "mechanical transmissibility of the human body in the z-direction."

In response to the needs of manufacturers and users, new work items were established, for example, classification of environmental vibration conditions, of concern to users and makers of sensitive equipment, including computers. Several new working groups were created, while others, having completed their tasks, were dissolved. The importance of cooperation and liaison between WG's and TC's was emphasized. A new joint working group, consisting of experts from TC 108 and TC 70 on Internal Combustion Engines, will be called into existence to standardize the measurement and evaluation of vibration of reciprocating machines. Also, the collaboration with IEC/SC50A in the development of procedures to assess the shock resistance of mechanical systems will be continued. In all, 30 resolutions pertaining to confirmation or upgrading of standards, establishment of new work items, and creation or dissolution of working groups were adopted at the closing plenary meeting of TC 108.

In the closing meeting, Rasa Rajeswaran, representative of the ISO Central Secretariat, expressed appreciation to NBS and to ANSI on behalf of all the delegates. The meeting was closed by William Rockwell, vice president of ANSI. The next plenary meeting is to be held in Shanghai, China, in September 1988.

M. R. Serbyn
Automated Production Technology Division
Center for Manufacturing Engineering
National Bureau of Standards
Gaithersburg, MD 20899